J. Fluid Mech. (2013), *vol.* 728, *pp.* 163–195. © Cambridge University Press 2013
doi:10.1017/jfm.2013.257

Solution of the flow over a non-uniform heavily loaded ducted actuator disk

R. Bontempo and M. Manna†

Dipartimento di Meccanica ed Energetica, Università degli Studi di Napoli Federico II, Via Claudio 21, 80125 Naples, Italy

(Received 12 December 2012; revised 7 May 2013; accepted 19 May 2013; first published online 5 July 2013)

The paper presents an extension to ducted rotors of the nonlinear actuator disk theory of Conway (*J. Fluid Mech.*, vol. 365, 1998, pp. 235–267) and it is exact for incompressible, axisymmetric and inviscid flows. The solution for the velocities and the Stokes stream function results from the superposition of ring vortices properly arranged along the duct surface and the wake region. Using a general analytical procedure the flow fields are given as a combination of one-dimensional integrals of expressions involving complete as well as incomplete elliptic integrals. The solution being exact, the proper shape of the slipstream whether converging or diverging is naturally accounted for, even for heavy loads. A semi-analytical method has been developed that enables the flow induced by an actuator disk housed in a contoured duct to be solved duly accounting for the nonlinear mutual interaction between the duct and the rotor. Non-uniform load distributions, rotor wake rotation and ducts of general shapes and thickness distribution can be dealt with. Thanks to its reduced numerical cost, the method is well suited for the design and/or analysis of ducted rotors for marine, wind and aeronautical applications.

Key words: aerodynamics, general fluid mechanics, mathematical foundations

1. Introduction

The concept of inserting a rotor into a duct is already very old, and it is currently used in the fields of propulsion and energy conversion systems for marine, wind and aeronautical applications. On general grounds, the duct enhances the performance of the coupled system by increasing either the efficiency of a heavily loaded propeller or the energy output of a turbine. Other applications aim at improving the cavitation behaviour of marine propellers.

Most of the theoretical investigations on ducted rotors are based on the combined use of several representations of the velocity field induced by the duct with that generated by the rotor, typically modelled by the lifting line, the lifting surface or the boundary element methods. Remarkable applications are due to Ryan & Glover (1972), Kerwin *et al.* (1987), Baltazar & Falcão de Campos (2009) and Çelik, Güner & Ekinci (2010), but this list should not be regarded as exhaustive. A more thorough literature review can be found in the textbooks of Breslin & Andersen (1994) and Carlton (2007). Not disregarding the computationally intensive three-dimensional unsteady computational fluid dynamics (CFD) based methods, in many applications the rotor

† Email address for correspondence: marcello.manna@unina.it

https://doi.org/10.1017/jfm.2013.257 Published online by Cambridge University Press

is still modelled as a linearized actuator disk (Horlock 1978; Conway 1995) with spanwise variable load or its nonlinear generalized variant (Wu 1962; Greenberg & Powers 1970; Conway 1998). Dickmann & Weissinger (1955) modelled a ducted propeller representing the duct with an elliptical distribution of ring vortices lying on a cylinder of constant radius and the propeller by an actuator disk of constant load. Chaplin (1964) and van Gunsteren (1973) investigated the effects of the slipstream contraction on the duct performance using simplified actuator disk models. Gibson & Lewis (1973) modelled a ducted propeller by coupling an actuator disk with a surface vorticity method. Although the rotation effects and the slipstream contraction were neglected, the duct was more closely represented by the localized surface vorticity distribution, compared to the thin aerofoil theory. Falcão de Campos (1983) calculated the axisymmetric flow through a ducted actuator disk in a wake using a discrete vortex sheet method.

The purpose of this paper is to extend the nonlinear actuator disk theory of Conway (1998) to ducted rotors in order to better fulfil the design and analysis needs for marine, wind and aeronautical applications. In more detail, an exact solution of the inviscid axisymmetric flow generated by a heavily loaded ducted rotor accounting for the proper shape of the slipstream, whether converging or diverging, is sought. Ideally, the solution procedure should be cost-effective, and capable of handling arbitrary load radial distributions, rotor wake rotation and ducts of general shape and thickness distribution.

This paper has been organized as follows. After this short introduction, in §§ 2 and 3 the models and the associated solutions for the open rotor and the duct-alone flows are detailed. In § 4 the differential problem governing the coupled flow is described; finally in §§ 5 and 6 the solution procedure and the results are presented.

2. The open rotor flow model

In order to simulate an open rotor and its vortical wake, consider the incompressible, steady and axisymmetric flow of an effectively inviscid fluid with vorticity through an actuator disk with centre at the origin of a cylindrical coordinate system (ζ, σ, θ), radius σ_{ad} and immersed in a free stream with velocity U_∞ in the positive ζ axis direction.

Preliminarily, the focus is on the characteristics of a general axisymmetric flow. As is customary when dealing with this class of problems, it is convenient to introduce the Stokes stream function Ψ, so that the mass-conservation equation is automatically satisfied. For the above flows, the velocity vector field $\boldsymbol{u} = (u, v, w)$ can be expressed in terms of a vector potential $\boldsymbol{B}$ through $\boldsymbol{u} = \boldsymbol{\nabla} \times \boldsymbol{B}$, with $B_\theta = \Psi/\sigma$. If $\boldsymbol{\nabla}(\boldsymbol{\nabla} \cdot \boldsymbol{B}) = \boldsymbol{0}$ then $\boldsymbol{B}$ satisfies the equation (Batchelor 1967)

$$\nabla^2 \boldsymbol{B} = -\boldsymbol{\omega}, \tag{2.1}$$

with $\boldsymbol{\omega}$ the vorticity vector

$$\boldsymbol{\omega} = (\omega_\zeta, \omega_\sigma, \omega_\theta) = \left(\frac{1}{\sigma} \frac{\partial(\sigma w)}{\partial \sigma}, -\frac{\partial w}{\partial \zeta}, \frac{\partial v}{\partial \zeta} - \frac{\partial u}{\partial \sigma} \right). \tag{2.2}$$

The θ component of (2.1) is equivalent to (Wu 1962; Batchelor 1967)

$$L_{(\sigma,\zeta)} \left(\frac{\Psi}{\sigma} \right) = \sigma \left(\frac{\partial^2}{\partial \sigma^2} + \frac{1}{\sigma} \frac{\partial}{\partial \sigma} - \frac{1}{\sigma^2} + \frac{\partial^2}{\partial \zeta^2} \right) \frac{\Psi}{\sigma} = \frac{\partial^2 \Psi}{\partial \sigma^2} - \frac{1}{\sigma} \frac{\partial \Psi}{\partial \sigma} + \frac{\partial^2 \Psi}{\partial \zeta^2} = -\omega_\theta \sigma. \tag{2.3}$$

https://doi.org/10.1017/jfm.2013.257 Published online by Cambridge University Press

Actually, since $\nabla(\nabla\cdot\boldsymbol{B})\cdot\boldsymbol{i}_\theta = 0$ for axisymmetric flow, (2.3) is always valid in this case. Alternatively, (2.3) can be found simply by substituting the axial and radial velocity expressions in terms of the Stokes stream function in the definition of ω_θ.

Denoting $H = p/\rho + (u^2 + v^2 + w^2)/2$, the momentum equation for steady incompressible inviscid flows, neglecting body forces, can be written as

$$\boldsymbol{u}\times\boldsymbol{\omega} = \nabla H \tag{2.4}$$

and used to manipulate the vorticity field appearing on the right-hand side of (2.1) or (2.3). From (2.4) it follows that $\boldsymbol{u}\cdot\nabla H = 0$, and therefore H is constant along a streamline and it is a function of Ψ alone, i.e. $H = H(\Psi)$. Thus using the chain rule

$$\nabla H = \nabla_{(\Psi)} H \boldsymbol{J}_\Psi = \frac{\mathrm{d}H}{\mathrm{d}\Psi}\nabla\Psi, \tag{2.5}$$

where $\nabla_{(\Psi)}H$ and $\boldsymbol{J}_\Psi$ are the gradient of H in the direction of Ψ and the Jacobian matrix of Ψ, respectively. Therefore (2.4) becomes

$$\boldsymbol{u}\times\boldsymbol{\omega} = \frac{\mathrm{d}H}{\mathrm{d}\Psi}\nabla\Psi. \tag{2.6}$$

Furthermore, the flow being axisymmetric, the θ component of (2.4) implies, with some lengthy, though straightforward, algebra, that the product σw is a function of Ψ alone too (Wu 1962). Therefore, to compute the vorticity field needed on the right-hand side of (2.3), it suffices to evaluate the cross-product between $\boldsymbol{u}$ and (2.6). The result, obtained with some remarkable algebra, reads

$$\boldsymbol{\omega} = (\omega_\zeta, \omega_\sigma, \omega_\theta) = \left(u\frac{\mathrm{d}(\sigma w)}{\mathrm{d}\Psi}, v\frac{\mathrm{d}(\sigma w)}{\mathrm{d}\Psi}, w\frac{\mathrm{d}(\sigma w)}{\mathrm{d}\Psi} - \sigma\frac{\mathrm{d}H}{\mathrm{d}\Psi}\right). \tag{2.7}$$

Recalling that the main objective is to simulate the axisymmetric flow induced by an open rotor and its vortical wake through an actuator disk, and keeping in mind that (2.3) is the governing equation to be solved, it is necessary to express the azimuthal component of the vorticity field $\omega_\theta(\zeta,\sigma)$ as a function of the load radial distribution $\mathscr{H}(\Psi) = \Delta H_{across\ disk} = H(\Psi)|_{(\zeta>0,\sigma<\sigma_s)} - H_\infty$ at the disk. In the previous relation, the quantity σ_s denotes the outer edge of the wake. Since outside the slipstream $H = H_\infty$, and inside it $H(\Psi)|_{(\zeta>0,\sigma<\sigma_s)} \neq H_\infty$, in the foregoing the subscript $(\zeta > 0, \sigma < \sigma_s)$ will be omitted when referring to $H(\Psi)$. Because $\mathscr{H}(\Psi)$ is a single-valued composite function of Ψ, although defined at the disk, it can be used everywhere in the slipstream. With the help of the angular momentum equation, $\mathscr{H}(\Psi)$ can be written as

$$\mathscr{H}(\Psi) = H(\Psi) - H_\infty = \Omega\sigma w, \tag{2.8}$$

where Ω is the angular velocity of the rotor. Finally, using (2.8) in (2.7), the θ component of the vorticity can be expressed as

$$-\omega_\theta\sigma = \begin{cases} \dfrac{\Omega^2\sigma^2 - \mathscr{H}}{\Omega^2}\dfrac{\mathrm{d}\mathscr{H}}{\mathrm{d}\Psi}, & \text{inside the slipstream,} \\ 0, & \text{outside the slipstream.} \end{cases} \tag{2.9}$$

https://doi.org/10.1017/jfm.2013.257 Published online by Cambridge University Press

Thus substituting (2.9) into (2.3) yields the following nonlinear partial differential equation with the associated conditions at infinity (Wu 1962):

$$L_{(\sigma,\zeta)}\left(\frac{\Psi}{\sigma}\right) = \begin{cases} \dfrac{\Omega^2\sigma^2 - \mathscr{H}}{\Omega^2}\dfrac{\mathrm{d}\mathscr{H}}{\mathrm{d}\Psi}, & \text{inside the slipstream,} \\ 0, & \text{outside the slipstream,} \end{cases} \tag{2.10}$$

$$\frac{1}{\sigma}\frac{\partial\Psi}{\partial\sigma} \to U_\infty, \quad \frac{\partial\Psi}{\partial\zeta} \to 0 \quad \text{as } \zeta \to -\infty \text{ or } \sigma \to \pm\infty, \tag{2.11a}$$

$$\frac{\partial\Psi}{\partial\zeta} \to 0 \quad \text{as } \zeta \to +\infty, \tag{2.11b}$$

valid outside the disk. To complete the problem formulation (2.10)–(2.11), the load distribution at the disk $\mathscr{H}(\Psi)$ and the angular velocity Ω have to be prescribed. However, the slipstream location $\sigma_s(\zeta)$, defining the domain region inside which the right-hand side of (2.10) does not vanish, is not known in advance and must be determined as part of the solution. For flows without swirl, that is, whenever the azimuthal velocity component $w(\zeta,\sigma)$ is zero in the wake region, the through-flow velocities $u(\zeta,\sigma)$ and $v(\zeta,\sigma)$ can be computed by solving problem (2.10)–(2.11) in terms of the Stokes stream function Ψ. Conversely, for swirled flows, the azimuthal velocity has to be computed using (2.8). It is worth noting that for prescribed $\mathscr{H}(\Psi)$ and Ω, problem (2.10)–(2.11) is fully decoupled from (2.8), and $w(\zeta,\sigma)$ can be evaluated from the field values of $\Psi(\zeta,\sigma)$.

Since $L_{(\zeta,\sigma)}$ is a linear operator, the differential equation (2.10) can be converted into the following nonlinear integral equation:

$$\frac{\Psi(\zeta,\sigma)}{\sigma} = \int_0^\infty \int_0^{\sigma_s(z)} G(\sigma, r, \zeta - z)\omega_\theta(z, r) r \,\mathrm{d}r \,\mathrm{d}z + q(\zeta,\sigma), \tag{2.12}$$

where $q(\zeta,\sigma)$ is a solution of $L_{(\zeta,\sigma)}\{q(\zeta,\sigma)\} = 0$. In (2.12), $G(\sigma, r, \zeta - z)$ is the Green function of the operator $L_{(\zeta,\sigma)}$ and satisfies

$$L_{(\zeta,\sigma)}\{G(\sigma, r, \zeta - z)\} = -\delta(\sigma - r)\delta(\zeta - z), \tag{2.13}$$

where δ is the Dirac delta function. From the conditions (2.11), it follows that $q(\zeta,\sigma) = U_\infty\sigma/2$ and $G(\sigma, r, \zeta - z)$ vanishes at infinity. A solution can be obtained by applying to (2.13) the Hankel transform with respect to σ (Wu 1962; Breslin & Andersen 1994):

$$G(\sigma, r, \zeta - z) = \frac{1}{2}\int_0^\infty \mathrm{e}^{-s|\zeta - z|}\,\mathrm{J}_1(sr)\mathrm{J}_1(s\sigma)\,\mathrm{d}s, \tag{2.14}$$

where J_1 is the Bessel function of the first kind. Finally, substituting (2.14) in (2.12), the solution of the problem (2.10)–(2.11) reduces to

$$\frac{\Psi(\zeta,\sigma)}{\sigma} = \frac{1}{2}\int_0^\infty \int_0^{\sigma_s(z)} \int_0^\infty \mathrm{e}^{-s|\zeta - z|}\omega_\theta(z, r) r\,\mathrm{J}_1(sr)\mathrm{J}_1(s\sigma)\,\mathrm{d}s\,\mathrm{d}r\,\mathrm{d}z + \frac{U_\infty\sigma}{2}. \tag{2.15}$$

Since the only non-zero component of the vorticity of the axisymmetric field $(u, v, 0)$ is ω_θ (see (2.2)), an alternative solution strategy for the problem (2.10)–(2.11) is based on the description of the wake by a continuous distribution of ring vortices with axis parallel to the ζ axis. To show the above, consider the stream function and velocity field induced by a single ring vortex of radius r, strength κ and located

https://doi.org/10.1017/jfm.2013.257 Published online by Cambridge University Press

at $\zeta = z$ and $\sigma = 0$, given by (Basset 1888; Lamb 1932)

$$\frac{\Psi'(\zeta,\sigma)}{\sigma} = \frac{\kappa r}{2}\int_0^\infty \mathrm{e}^{-s|\zeta-z|}\,\mathrm{J}_1(sr)\mathrm{J}_1(s\sigma)\,\mathrm{d}s, \tag{2.16}$$

$$u'(\zeta,\sigma) = \frac{\kappa r}{2}\int_0^\infty \mathrm{e}^{-s|\zeta-z|}s\,\mathrm{J}_1(sr)\mathrm{J}_0(s\sigma)\,\mathrm{d}s, \tag{2.17}$$

$$v'(\zeta,\sigma) = \pm\frac{\kappa r}{2}\int_0^\infty \mathrm{e}^{-s|\zeta-z|}s\,\mathrm{J}_1(sr)\mathrm{J}_1(s\sigma)\,\mathrm{d}s, \tag{2.18}$$

where the positive sign is for $\zeta - z \geqslant 0$ and vice versa. This simple flow solution can be used to reproduce a vortical region, like the wake. To this aim, it is necessary to introduce a continuum surface singularity distribution covering the space region bounded by the disk and the slipstream $\sigma_s(\zeta)$. Defining $\gamma_{ad}(\zeta,\sigma)$ as the ring vortex density strength and integrating equations (2.16)–(2.18) over the wake leads to the following expressions for the overall flow:

$$\frac{\Psi(\zeta,\sigma)}{\sigma} = \frac{1}{2}\int_0^\infty\int_0^{\sigma_s(z)}\int_0^\infty \mathrm{e}^{-s|\zeta-z|}\gamma_{ad}(z,r)r\,\mathrm{J}_1(sr)\mathrm{J}_1(s\sigma)\,\mathrm{d}s\,\mathrm{d}r\,\mathrm{d}z + \frac{U_\infty\sigma}{2}, \tag{2.19}$$

$$u(\zeta,\sigma) = \frac{1}{2}\int_0^\infty\int_0^{\sigma_s(z)}\int_0^\infty \mathrm{e}^{-s|\zeta-z|}\gamma_{ad}(z,r)sr\,\mathrm{J}_1(sr)\mathrm{J}_0(s\sigma)\,\mathrm{d}s\,\mathrm{d}r\,\mathrm{d}z + U_\infty, \tag{2.20}$$

$$v(\zeta,\sigma) = \pm\frac{1}{2}\int_0^\infty\int_0^{\sigma_s(z)}\int_0^\infty \mathrm{e}^{-s|\zeta-z|}\gamma_{ad}(z,r)sr\,\mathrm{J}_1(sr)\mathrm{J}_1(s\sigma)\,\mathrm{d}s\,\mathrm{d}r\,\mathrm{d}z. \tag{2.21}$$

The density function $\gamma_{ad}(\zeta,\sigma)$ has to be capable of reproducing the vorticity field $\omega_\theta(\zeta,\sigma)$ imposed by the disk load distribution $\mathscr{H}(\Psi)$. Comparing (2.15) and (2.19), it is readily understood that (2.19) satisfies problem (2.10)–(2.11) whenever (Conway 1998)

$$\gamma_{ad}(\zeta,\sigma) = \omega_\theta(\zeta,\sigma). \tag{2.22}$$

In conclusion, once the load distribution $\mathscr{H}(\Psi)$ and the angular velocity Ω have been chosen, the through flow can be described by a ring vortex distribution of strength $\gamma_{ad}(\zeta,\sigma) = \omega_\theta(\zeta,\sigma)$, while the tangential velocity is given by (2.8).

3. The duct-alone flow model

As anticipated in § 1, the main task of the duct is to enhance the performance of the rotor whether it operates as a propeller or as a turbine. It is generally a slender lifting element defining a contoured axisymmetric channel inside which the rotor is installed.

Following the classical approach of Martensen (1959), later elaborated by Jacob & Riegels (1963), Wilkinson (1967*a*,*b*) and Nyiri & Baranyi (1983), the inviscid flow around an axisymmetric duct of general shape is assumed to be described by a sheet of ring vorticity whose density strength γ_d makes the duct boundary a stream surface. An extensive description of the method and many related applications can be found in Lewis (1991, and references therein). Only the key elements of the procedure are summarized hereafter.

Since the flow at zero incidence around an annular body with contour C is axisymmetric, it is again convenient to introduce a cylindrical coordinate system (ζ,σ,θ). The objective is to determine the density strength γ_d that satisfies the appropriate velocity boundary condition along solid walls, i.e. $\boldsymbol{u}\cdot\boldsymbol{n} = 0$, with $\boldsymbol{n}$ the

https://doi.org/10.1017/jfm.2013.257 Published online by Cambridge University Press

outward unit normal. In turn, the γ_p distribution is related to the circulation around the duct by

$$\Gamma = \oint_C \gamma_d(c)\,\mathrm{d}c, \tag{3.1}$$

which controls the amount of lift around the duct cross-section. In (3.1), c is the curvilinear abscissa measured clockwise from the leading edge.

It can be shown (see e.g. Lewis 1991; Anderson 2001) that γ_d is also the jump in the tangential velocity across the vortex sheet

$$\gamma_d(c) = (\boldsymbol{u}_a(c) - \boldsymbol{u}_b(c)) \cdot \boldsymbol{t}, \tag{3.2}$$

where $\boldsymbol{t}$ is the unit vector tangent to the duct surface, and $\boldsymbol{u}_a$ and $\boldsymbol{u}_b$ are the velocities just above and beneath the vorticity sheet, respectively. Moreover, it can be further shown (Martensen 1959; Lewis 1991) that the no-penetration requirement along the solid wall is satisfied by the homogeneous Dirichlet boundary condition on the tangent to the wall velocity just beneath the vorticity sheet $\boldsymbol{u}_b(c)$, provided there are no vortex or source distributions within the profile. Using the homogeneous Dirichlet boundary condition in (3.2), it follows that the solution γ_d equals the velocity parallel to the annular surface just above the sheet.

In more detail, the $\gamma_d(c)$ distribution can be computed by solving the following Fredholm integral equation of the second kind (Lewis 1991):

$$-\frac{1}{2}\gamma_d(c) + \oint_C k(c,\tilde{c})\gamma_d(\tilde{c})\,\mathrm{d}\tilde{c} + U_\infty \cos\beta(c) = 0. \tag{3.3}$$

In the above equation, $\beta(c)$ is the local profile slope and $k(c,\tilde{c})$ is the velocity parallel to the surface, at c, induced by a ring vortex of unit strength located at $\tilde{c}$. The first term in (3.3) is precisely half the velocity jump across the sheet, the second is the velocity induced in c by all the duct vortices, and the third is the contribution of U_∞ in the tangent to the wall direction.

A classical result of the potential flow theory is that for a given body there is an infinite number of valid theoretical solutions, one for each value of the total circulation Γ. Therefore, the method discussed above for the description of the flow around an annular wing must be complemented by an additional condition fixing Γ. In order to mimic the lifting behaviour induced by the viscosity in the inviscid formulation, the circulation Γ has to make the flow leave the duct smoothly at the trailing edge, according to the well-known Kutta condition. In conclusion, the $\gamma_d(c)$ distribution has to satisfy (3.3) and the Kutta condition at the trailing edge as well.

It is worth noting that an equivalent formulation of the present problem in terms of the stream function Ψ_d induced by the duct ring vortex sheet is obtained by associating the conditions at infinity and the no-penetration requirement along the solid wall contour C to the elliptic equation (2.3) having set its right-hand side to zero:

$$L_{(\sigma,\xi)}\left(\frac{\Psi_d}{\sigma}\right) = 0, \tag{3.4}$$

$$\frac{1}{\sigma}\frac{\partial \Psi_d}{\partial \sigma} \to U_\infty, \quad \frac{\partial \Psi_d}{\partial \zeta} \to 0 \quad \text{at infinity,} \tag{3.5a}$$

$$\Psi_d = \Psi_0 = \text{const.} \quad \text{on } C. \tag{3.5b}$$

https://doi.org/10.1017/jfm.2013.257 Published online by Cambridge University Press

Owing to the linearity of problem (3.4)–(3.5), its solution can be expressed as the superposition of an infinite number of ring vortices (equation (2.16)) forming a sheet:

$$\frac{\Psi_d(\zeta,\sigma)}{\sigma}=\frac{1}{2}\oint_C\int_0^\infty \gamma_d(c)r(c)\mathrm{e}^{-s|\zeta-z|}\,\mathrm{J}_1(sr(c))\mathrm{J}_1(s\sigma)\,\mathrm{d}s\,\mathrm{d}c+\frac{U_\infty\sigma}{2}. \tag{3.6}$$

Clearly, in the above equation, the $\gamma_d(c)$ distribution has to satisfy the boundary condition (3.3) and the Kutta condition.

4. The coupled flow model

With the assumptions adopted in §§ 2 and 3, the differential problem (2.10)–(2.11) applies as well to the case of a ducted rotor, provided the appropriate no-penetration boundary condition on the profile is enforced:

$$L_{(\zeta,\sigma)}\left(\frac{\Psi}{\sigma}\right)=\begin{cases}\dfrac{\Omega^2\sigma^2-\mathscr{H}}{\Omega^2}\dfrac{\mathrm{d}\mathscr{H}}{\mathrm{d}\Psi}, & \text{inside the slipstream,}\\ 0, & \text{outside the slipstream,}\end{cases} \tag{4.1}$$

$$\frac{1}{\sigma}\frac{\partial\Psi}{\partial\sigma}\to U_\infty,\quad \frac{\partial\Psi}{\partial\zeta}\to 0 \quad \text{as } \zeta\to-\infty \text{ or } \sigma\to\pm\infty, \tag{4.2a}$$

$$\frac{\partial\Psi}{\partial\zeta}\to 0 \quad \text{as } \zeta\to+\infty, \tag{4.2b}$$

$$\Psi=\Psi_0=\text{const.} \quad \text{on } C. \tag{4.2c}$$

Comparing (4.1)–(4.2) with (2.10)–(2.11), an additional difficulty arises, in that a new boundary condition has to be satisfied. Similarly to the slipstream position $\sigma_s(\zeta)$, the unknown value Ψ_0 has also to be evaluated as part of the solution. The solution of (4.1)–(4.2) in terms of stream function can again be expressed in the form (2.12), with an appropriate value of $q(\zeta,\sigma)$ according to the new boundary condition (4.2*c*). As already stated, Ψ_d satisfies $L_{(\zeta,\sigma)}\{\Psi_p(\zeta,\sigma)/\sigma\}=0$ and the associated conditions at infinity. Therefore, $q(\zeta,\sigma)$ coincides with $\Psi_d(\zeta,\sigma)/\sigma$, provided the density strength vortex distribution γ_d is computed by enforcing on the duct boundary the no-penetration condition. Owing to the presence of the actuator disk, the latter condition can be expressed as

$$-\frac{1}{2}\gamma_d(c)+\oint_C k(c,\tilde{c})\gamma_d(\tilde{c})\,\mathrm{d}\tilde{c}+(U_\infty+u(c))\cos\beta(c)+v(c)\sin\beta(c)=0. \tag{4.3}$$

Equation (4.3) is equivalent to (3.3) except for the presence of the $u(c)$ and $v(c)$ terms representing the velocities induced by the actuator disk at c on the profile, evaluated through (2.20)–(2.21). Finally, the coupled flow solution corresponding to (2.19), using (3.6), reads

$$\begin{aligned}\frac{\Psi(\zeta,\sigma)}{\sigma}=&\frac{1}{2}\int_0^\infty\int_0^{\sigma_s(z)}\int_0^\infty \mathrm{e}^{-s|\zeta-z|}\gamma_{ad}(z,r)r\,\mathrm{J}_1(sr)\mathrm{J}_1(s\sigma)\,\mathrm{d}s\,\mathrm{d}r\,\mathrm{d}z\\ &+\underbrace{\frac{1}{2}\oint_C\int_0^\infty \gamma_d(c)r(c)\mathrm{e}^{-s|\zeta-z|}\,\mathrm{J}_1(sr(c))\mathrm{J}_1(s\sigma)\,\mathrm{d}s\,\mathrm{d}c+\frac{U_\infty\sigma}{2}}_{\dfrac{\Psi_d(\zeta,\sigma)}{\sigma}}.\end{aligned} \tag{4.4}$$

https://doi.org/10.1017/jfm.2013.257 Published online by Cambridge University Press

Comparing (2.19) and (4.4) it turns out that, in addition to the terms associated with the wake ring vortex distribution and to the free stream, a new contribution to the stream function, provided by the duct ring vortex sheet, appears. Similarly to (2.19), equation (4.4) represents the exact flow solution of the coupled problem.

5. Solution strategy

In § 4 it has been shown that (4.4) is the exact coupled flow solution in the whole field. However, the direct evaluation of Ψ via (4.4) is prevented due to the implicitness of the solution. The implicitness is three-fold. Firstly, the slipstream location $\sigma_s(\zeta)$ depends upon the stream function field Ψ and moreover it is unknown. Secondly, the unknown density strength γ_{ad}, or else the angular component of the vorticity (see equation (2.22)), is also a function of the disk load $\mathscr{H}(\Psi)$ and thus of Ψ. Thirdly, differently from the open rotor formulation, the new term Ψ_d itself depends upon Ψ through u_m and v_m.

One way to approach the problem consists in specifying *a priori* the load distribution at the disk in terms of Ψ, since by so doing the γ_{ad} or else ω_θ in (4.4) can also be expressed as a function of Ψ through (2.9). Assuming now that the load is a continuous function, a suitable polynomial approximation to arbitrary accuracy is (Conway 1998)

$$\mathscr{H}(\Psi) = \sum_{m=0}^{M} a_m \left(\frac{\Psi}{\Psi_{\sigma_{ad}}} \right)^m, \tag{5.1}$$

where $\Psi_{\sigma_{ad}}$ is the stream function evaluated at $(\zeta = 0, \sigma = \sigma_{ad})$. It can be simply proved that $\mathscr{H}(0) = a_0$ and, if the load distribution falls to zero at the slipstream edge, i.e. $\mathscr{H}(\Psi_{\sigma_{ad}}) = 0$, then $\sum_{m=0}^{M} a_m = 0$. Obviously, if $\mathscr{H}(0) = 0$, then $\sum_{m=1}^{M} a_m = 0$. Using (5.1) and further assuming the load $\mathscr{H}(\Psi)$ to be C^1 continuous, the θ component of the vorticity inside the slipstream (equation (2.9)) becomes

$$\frac{\omega_\theta(\zeta,\sigma)}{\sigma} = \left[\frac{J^2}{\pi^2 U_\infty^2} \left(\frac{\sigma_{ad}}{\sigma} \right)^2 \sum_{m=0}^{M} a_m \left(\frac{\Psi}{\Psi_{\sigma_{ad}}} \right)^m - 1 \right] \sum_{m=1}^{M} \frac{m a_m}{\Psi_{\sigma_{ad}}} \left(\frac{\Psi}{\Psi_{\sigma_{ad}}} \right)^{m-1}. \tag{5.2}$$

In the above equation, the advance coefficient J is defined as $J = U_\infty / nD$, where D is the rotor diameter and n is the rotational speed. The advance coefficient J is typically used in the propeller field, while the tip speed ratio $\lambda = \Omega \sigma_{ad} / U_\infty$ is the typical turbine rotation parameter. The previous and the following equations can be expressed in terms of λ simply by substituting $J = \pi/\lambda$. In view of the exact integration of (4.4), it is convenient to express the tangential vorticity as a function of σ and ζ, a task that can be accomplished using the following polynomial expansion (Conway 1998):

$$\frac{\omega_\theta(\zeta,\sigma)}{\sigma} = \sum_{n=0}^{N} A_n(\zeta) \left[1 - \left(\frac{\sigma}{\sigma_s(\zeta)} \right)^2 \right]^n. \tag{5.3}$$

Evaluating (5.2) and (5.3) along the slipstream edge, it can be readily shown that the value of the first coefficient in (5.2) is $A_0 = -\sum_{m=1}^{M} m a_m / \Psi_{\sigma_{ad}}$. Applying the change of variable $x = r/\sigma_s(z)$ to (4.4), the radial integral can be cast in the form

$$\int_0^1 x^{\nu+1} (1 - x^2)^\mu \mathrm{J}_\nu(bx)\, \mathrm{d}x = 2^\mu \Gamma(\mu + 1) b^{-(\mu+1)} \mathrm{J}_{\nu+\mu+1}(b), \tag{5.4}$$

https://doi.org/10.1017/jfm.2013.257 Published online by Cambridge University Press

whose exact solution, appearing on the right-hand side of (5.4), is due to Sonine (1880). With the help of (5.4) and (2.22), equations (4.4), (2.20) and (2.21) become

$$\Psi(\zeta,\sigma) = \sigma \int_0^\infty \sum_{n=0}^{N} A_n(z) 2^{n-1} n! \sigma_s^{2-n}(z) I_{(-(n+1),n+2,1)}(\sigma_s(z),\sigma,\zeta - z)\,\mathrm{d}z + \Psi_d(\zeta,\sigma), \tag{5.5}$$

$$u(\zeta,\sigma) = \int_0^\infty \sum_{n=0}^{N} A_n(z) 2^{n-1} n! \sigma_s^{2-n}(z) I_{(-n,n+2,0)}(\sigma_s(z),\sigma,\zeta - z)\,\mathrm{d}z + U_\infty, \tag{5.6}$$

$$v(\zeta,\sigma) = \pm \int_0^\infty \sum_{n=0}^{N} A_n(z) 2^{n-1} n! \sigma_s^{2-n}(z) I_{(-n,n+2,1)}(\sigma_s(z),\sigma,\zeta - z)\,\mathrm{d}z. \tag{5.7}$$

The integrals $I_{(\xi,\mu,\nu)}$ appearing in (5.5)–(5.7), with ξ, μ and ν integers, are of the type

$$I_{(\xi,\mu,\nu)} = \int_0^\infty \mathrm{e}^{-s|\zeta - z|} s^\xi \mathrm{J}_\mu(sr)\mathrm{J}_\nu(s\sigma)\,\mathrm{d}s \tag{5.8}$$

and can be expressed in terms of complete elliptic integrals and the Heuman Lambda function through the recursive scheme detailed in Conway (2000).

Furthermore (5.5) requires the evaluation of the duct contribution $\Psi_d(\zeta,\sigma)$ through (3.6). As anticipated, the density strength $\gamma_d(c)$ appearing in (3.6) has to be computed by making the duct boundary a stream surface. In the coupled flow case, this is obtained by satisfying (4.3), as explained in § 4. For a body of arbitrary shape there is no closed-form analytical solution for $\gamma_d(c)$; rather, the solution must be obtained numerically. Following the classical panel method approach, the discrete counterpart of (4.3) is obtained by approximating the curvilinear integral with a quadrature rule, thus dividing the profile into M_p panels with length Δc_n. The panels are spaced such that pivotal points on the upper and lower surface lie directly opposite to one another in pairs. Using the trapezium rule yields the following system of $M_p \times M_p$ linear algebraic equations:

$$\begin{cases} \displaystyle\sum_{n=1}^{M_p} \boldsymbol{K}(c_1,c_n)\gamma_d(c_n) = -(U_\infty + u_1)\cos\beta_1 - v_1 \sin\beta_1, \\ \displaystyle\sum_{n=1}^{M_p} \boldsymbol{K}(c_2,c_n)\gamma_d(c_n) = -(U_\infty + u_2)\cos\beta_2 - v_2 \sin\beta_2, \\ \qquad\qquad \vdots \\ \displaystyle\sum_{n=1}^{M_p} \boldsymbol{K}(c_m,c_n)\gamma_d(c_n) = -(U_\infty + u_m)\cos\beta_m - v_m \sin\beta_m, \\ \qquad\qquad \vdots \\ \displaystyle\sum_{n=1}^{M_p} \boldsymbol{K}(c_{M_p},c_n)\gamma_d(c_n) = -(U_\infty + u_{M_p})\cos\beta_{M_p} - v_{M_p} \sin\beta_{M_p}. \end{cases} \tag{5.9}$$

In the above equations, u_m and v_m have to be evaluated through (5.6)–(5.7), while the entries of matrix $\boldsymbol{K}$ are equal to $k(c_m,c_n)\Delta c_n$ when $n \neq m$ and $k(c_m,c_m)\Delta c_m - \gamma_d(c_m)/2$ for $n = m$. Therefore, the coefficients $\boldsymbol{K}(c_m,c_n)$ may be interpreted as the tangent to

https://doi.org/10.1017/jfm.2013.257 Published online by Cambridge University Press

the wall velocity induced at c_m by the ring vortex of unit strength located at c_n. Thus, denoting by u_{mn} and v_{mn} the axial and radial velocities due to the unit-strength ring vortex, the $\boldsymbol{K}(c_m, c_n)$ coefficients are (Gibson 1972)

$$\boldsymbol{K}(c_m, c_n) = (u_{mn}\cos\beta_m + v_{mn}\sin\beta_m)\Delta c_n, \tag{5.10}$$

with

$$u_{mn} = -\frac{1}{2\pi\sigma_n\sqrt{\zeta^{*2} + (\sigma^* + 1)^2}}\left\{\mathrm{K(k)} - \left[1 + \frac{2(\sigma^* - 1)}{\zeta^{*2} + (\sigma^* - 1)^2}\right]\mathrm{E(k)}\right\}, \tag{5.11a}$$

$$v_{mn} = \frac{\zeta^*/\sigma^*}{2\pi\sigma_n\sqrt{\zeta^{*2} + (\sigma^* + 1)^2}}\left\{\mathrm{K(k)} - \left[1 + \frac{2\sigma^*}{\zeta^{*2} + (\sigma^* - 1)^2}\right]\mathrm{E(k)}\right\}. \tag{5.11b}$$

In the above equations, K(k) and E(k) are complete elliptic integrals of the first and second kind, $\mathrm{k} = \sqrt{4\sigma^*/[\zeta^{*2} + (\sigma^* + 1)^2]}$, $\sigma^* = \sigma_m/\sigma_n$ and $\zeta^* = (\zeta_m - \zeta_n)/\sigma_n$.

As proven in Martensen (1959), the matrix $\boldsymbol{K}$ is nearly singular. Moreover, the trapezoidal integration in the mth equation is reasonably accurate except for those element pairs formed with the subset of points lying on the opposite surface in closest proximity to point m (see Wilkinson (1967*a*) for details). There the integrand has a high and narrow peak, the area of which is typically overestimated by the trapezium rule method. To overcome this problem, the so-called back-diagonal correction, first proposed by Jacob & Riegels (1963), is used (see also Wilkinson (1967*a*) and Lewis (1991)). The technique operates on the back-diagonal of the matrix $\boldsymbol{K}$, i.e. on the coefficients $\boldsymbol{K}(c_i, c_{M_p+1-i})$ with $i = 1, \ldots, M_p$, to account for the quadrature errors. Specifically, it requires that the coupling coefficients opposite to point c_m with $m = 1, \ldots, M_p$, i.e. $\boldsymbol{K}(c_{M_p+1-m}, c_m)$, are replaced by a mean value derived by the condition of irrotationality in the inner of the profile:

$$\sum_{n=1}^{M_p} \boldsymbol{K}(c_n, c_m)\Delta c_n = 0, \quad m = 1, \ldots, M_p. \tag{5.12}$$

A detailed proof of (5.12) can be found in Lewis (1991). Using (5.12) the opposite coupling coefficients, which lie on the back diagonal of the matrix $\boldsymbol{K}$, have to be replaced with

$$\boldsymbol{K}(c_{M_p+1-m}, c_m) = -\frac{1}{\Delta c_{M_p+1-m}} \sum_{\substack{n=1 \\ n\neq M_p+1-m}}^{M_p} \boldsymbol{K}(c_n, c_m)\Delta c_n, \quad m = 1, \ldots, M_p, \tag{5.13}$$

ensuring that the net circulation around the profile interior, implied by the numerical model, is made to be zero. The outcome of this procedure is a singular matrix because, from (5.13), it can be inferred that the sum of all equations, each being first multiplied in turn by the constant Δc_n, is now zero. The indeterminacy stems from the fact that, unless the total circulation Γ is enforced, an infinity of solutions is possible. The value of the total circulation Γ can be fixed through the discrete counterpart of (3.1):

$$\Gamma = \sum_{n=1}^{M_p} \gamma_d(c_n)\Delta c_n. \tag{5.14}$$

https://doi.org/10.1017/jfm.2013.257 Published online by Cambridge University Press

As already mentioned, once the back diagonal correction is applied, system (5.9) becomes singular and one of its equations can be dropped and replaced with (5.14). Equivalently Lewis (1991) suggests to add (5.14) to all equations (5.9), thus obtaining

$$\begin{cases} \displaystyle\sum_{n=1}^{M_p} (\boldsymbol{K}(c_1, c_n) + \Delta c_n)\gamma_d(c_n) = -(U_\infty + u_1)\cos\beta_1 - v_1 \sin\beta_1 + \Gamma, \\ \displaystyle\sum_{n=1}^{M_p} (\boldsymbol{K}(c_2, c_n) + \Delta c_n)\gamma_d(c_n) = -(U_\infty + u_2)\cos\beta_2 - v_2 \sin\beta_2 + \Gamma, \\ \qquad\qquad \vdots \\ \displaystyle\sum_{n=1}^{M_p} (\boldsymbol{K}(c_m, c_n) + \Delta c_n)\gamma_d(c_n) = -(U_\infty + u_m)\cos\beta_m - v_m \sin\beta_m + \Gamma, \\ \qquad\qquad \vdots \\ \displaystyle\sum_{n=1}^{M_p} (\boldsymbol{K}(c_{M_p}, c_n) + \Delta c_n)\gamma_d(c_n) = -(U_\infty + u_{M_p})\cos\beta_{M_p} - v_{M_p} \sin\beta_{M_p} + \Gamma. \end{cases} \tag{5.15}$$

For any given value of the circulation Γ, the above system can be solved. However, in general, the circulation Γ that makes the flow leave the duct smoothly at the trailing edge is not known in advance. Following Wilkinson (1967*a*), the Kutta condition is imposed requiring that the static pressure, and therefore the surface vorticity, at the two trailing edge elements on the upper and lower surfaces have the same magnitude. So the vorticity strength of the panel just before and just after the trailing edge are related by

$$\gamma_d(c_{te}) = -\gamma_d(c_{te+1}). \tag{5.16}$$

For smooth flow leaving the trailing edge, $\gamma_d(c_{te})$ must be clockwise and $\gamma_d(c_{te+1})$ vice versa. This is the reason for the negative sign in (5.16). To eliminate the unknown Γ from (5.15), it is possible to replace it by two separate systems, one for the uniform and actuator disk stream and one for the bound vortex strength:

$$\begin{cases} \displaystyle\sum_{n=1}^{M_p} (\boldsymbol{K}(c_1, c_n) + \Delta c_n)\gamma_{d,1}(c_n) = -(U_\infty + u_1)\cos\beta_1 - v_1 \sin\beta_1, \\ \displaystyle\sum_{n=1}^{M_p} (\boldsymbol{K}(c_2, c_n) + \Delta c_n)\gamma_{d,1}(c_n) = -(U_\infty + u_2)\cos\beta_2 - v_2 \sin\beta_2, \\ \qquad\qquad \vdots \\ \displaystyle\sum_{n=1}^{M_p} (\boldsymbol{K}(c_m, c_n) + \Delta c_n)\gamma_{d,1}(c_n) = -(U_\infty + u_m)\cos\beta_m - v_m \sin\beta_m, \\ \qquad\qquad \vdots \\ \displaystyle\sum_{n=1}^{M_p} (\boldsymbol{K}(c_{M_p}, c_n) + \Delta c_n)\gamma_{d,1}(c_n) = -(U_\infty + u_{M_p})\cos\beta_{M_p} - v_{M_p} \sin\beta_{M_p}, \end{cases} \tag{5.17a}$$

https://doi.org/10.1017/jfm.2013.257 Published online by Cambridge University Press

$$\begin{cases} \sum_{n=1}^{M_p} (\boldsymbol{K}(c_1, c_n) + \Delta c_n)\gamma_{d,2}(c_n) = 1, \\ \sum_{n=1}^{M_p} (\boldsymbol{K}(c_2, c_n) + \Delta c_n)\gamma_{d,2}(c_n) = 1, \\ \qquad\qquad \vdots \\ \sum_{n=1}^{M_p} (\boldsymbol{K}(c_m, c_n) + \Delta c_n)\gamma_{d,2}(c_n) = 1, \\ \qquad\qquad \vdots \\ \sum_{n=1}^{M_p} (\boldsymbol{K}(c_{M_p}, c_n) + \Delta c_n)\gamma_{d,2}(c_n) = 1, \end{cases} \tag{5.17b}$$

where

$$\gamma_d(c_n) = \gamma_{d,1}(c_n) + \Gamma\gamma_{d,2}(c_n). \tag{5.18}$$

The same coefficient matrix is applicable to both sets of equations, thus demanding no additional major computing cost. Independent solutions for $\gamma_{d,1}(c_n)$ and $\gamma_{d,2}(c_n)$ can be obtained from (5.17*a*) and (5.17*b*). Then, on substituting (5.18) in (5.16), the value of the circulation Γ that satisfies the Kutta condition is computed through

$$\Gamma = -\frac{\gamma_{d,1}(c_{te}) + \gamma_{d,1}(c_{te+1})}{\gamma_{d,2}(c_{te}) + \gamma_{d,2}(c_{te+1})}. \tag{5.19}$$

The density strengths $\gamma_{d,1}(c_n)$ and $\gamma_{d,2}(c_n)$ are subsequently recombined in (5.18) to give the overall vorticity density strength distribution $\gamma_d(c_n)$, which can be used to compute the duct contribution $\Psi_d(\zeta, \sigma)$ through (3.6). The latter, on performing the inner integral (Gradshteyn & Ryzhik 1980) and then using the trapezium rule, becomes

$$\Psi_d(\zeta, \sigma) = \sum_{m=1}^{M_P} \frac{\gamma_d(c_m)\Delta c_m\sqrt{\sigma\sigma_m}}{2\pi} \mathrm{Q}_{1/2}(\omega_m) + \frac{U_\infty\sigma^2}{2}, \tag{5.20}$$

where $\mathrm{Q}_{1/2}$ is the Legendre function of the second kind and ω_m is given by $\omega_m = 1 + [(\sigma_m - \sigma)^2 + (\zeta - \zeta_m)^2]/(2\sigma_m\sigma)$.

The integration of (5.5)–(5.7) still requires knowledge of $\sigma_s(\zeta)$. Since, on the slipstream boundary, the Stokes stream function is constant and equal to $\Psi(0, \sigma_{ad})$, then (5.5) reduces there to the following nonlinear integral equation for $\sigma_s(\zeta)$:

$$\Psi(0, \sigma_{ad}) = \sigma_s(\zeta) \int_0^\infty \sum_{n=0}^{N} A_n(z) 2^{n-1} n! \sigma_s^{2-n}(z) I_{(-(n+1),n+2,1)}(\sigma_s(z), \sigma_s(z), \zeta - z)\, \mathrm{d}z + \frac{U_\infty\sigma_s^2(\zeta)}{2} + \Psi_d'(\zeta, \sigma_s(\zeta)), \tag{5.21}$$

with $\Psi_d' = \Psi_d - (U_\infty\sigma^2)/2$, to be solved iteratively. The solution procedure begins by computing and storing in a pre-processing stage the LU decomposition of the coefficient matrix $\boldsymbol{K}$ that appears in (5.17), which merely depends upon the duct geometry. Subsequently, the $\gamma_{d,2}(c_m)$ distribution is evaluated once by (5.17*b*). Assume

https://doi.org/10.1017/jfm.2013.257 Published online by Cambridge University Press

now that provisional values of $\sigma_s(\zeta)$ and $\{A_n\}_{n=0,N}$ are available within the wake, for instance from the previous iteration. Likewise, assume provisional values of $\gamma_d(c_m)$ on the profile are available. Then the Stokes stream function in the wake can be evaluated through (5.5) by performing the integration in the axial direction numerically. Next, the tangential vorticity field can be computed with (5.2) and parametrized with (5.3) through a new set of $\{A_n\}_{n=0,N}$, selected with the help of a least-squares minimization procedure. Then from (5.6) and (5.7) the axial and radial velocities induced by the actuator disk on the profile are evaluated, and the right-hand side of (5.17*a*) and consequently $\gamma_{d,1}(c_m)$ are updated. After that, the Kutta condition is enforced through (5.19) and a new value of $\gamma_d(c_m)$ results from (5.18). Finally, from (5.21), the new $\sigma_s(\zeta)$ is

$$\sigma_s(\zeta) = \sqrt{\left(\frac{\Psi_d'(\zeta, \sigma_s(\zeta))}{\sigma_s(\zeta) U_\infty} + \frac{I(\zeta, \sigma_s(\zeta))}{U_\infty}\right)^2 + \frac{2\Psi(0, \sigma_{ad})}{U_\infty}} - \frac{\Psi_d'(\zeta, \sigma_s(\zeta))}{\sigma_s(\zeta) U_\infty} - \frac{I(\zeta, \sigma_s(\zeta))}{U_\infty}, \tag{5.22}$$

where

$$I(\zeta, \sigma_s(\zeta)) = \int_0^\infty \sum_{n=0}^{N} A_n(z) 2^{n-1} n! \sigma_s^{2-n}(z) I_{(-(n+1),n+2,1)}(\sigma_s(z), \sigma_s(z), \zeta - z)\, \mathrm{d}z. \tag{5.23}$$

At the first iteration $\gamma_d(c_m)$, $\sigma_s(\zeta)$ and Ψ are calculated ignoring the presence of the disk.

From an engineering point of view, it would definitely be preferable to specify the radial distribution of the disk load $\mathscr{H}(\sigma)$. However, on physical grounds, the existence of a one-to-one correspondence between $\mathscr{H}(\sigma)$ and $\mathscr{H}(\Psi)$ is conjectured, and therefore it is always possible to prescribe $\mathscr{H}(\sigma)$ and then to evaluate the associated $\mathscr{H}(\Psi)$; for example, it is possible to prescribe $\mathscr{H}(\sigma)$ at the disk and then to update the coefficient a_m in (5.1) to match $\mathscr{H}(\sigma)$ at each iteration (Conway 1998).

6. Results and applications

The method described in the previous sections provides the values of all physical quantities needed to evaluate the performance parameters of the device, namely the thrust coefficient C_T and the power coefficient C_P. Moreover, another very important performance coefficient, typically employed in the propeller field, is the propulsive efficiency, $\eta = C_T/C_P$. In particular, integrating the static pressure jump $\Delta p_{ad}(\sigma)$ across the actuator disk and the power over the rotor plane yields

$$C_{T,rot} = \frac{T_{rot}}{\frac{1}{2}\pi\rho U_\infty^2 \sigma_{ad}^2} = \frac{1}{\frac{1}{2}\pi\rho U_\infty^2 \sigma_{ad}^2} \int_0^{\sigma_{ad}} \Delta p_{ad}(\sigma) 2\pi\sigma\, \mathrm{d}\sigma, \tag{6.1}$$

$$C_P = \frac{P}{\frac{1}{2}\pi\rho U_\infty^3 \sigma_{ad}^2} = \frac{1}{\frac{1}{2}\pi\rho U_\infty^3 \sigma_{ad}^2} \int_0^{\sigma_{ad}} \mathscr{H}(0, \sigma) \rho u(0, \sigma) 2\pi\sigma\, \mathrm{d}\sigma, \tag{6.2}$$

where T_{rot} and P are the axial force and the power experienced by the rotor. In the following, quantities denoted with a hat ($\widehat{\ }$) are made dimensionless using the reference length σ_{ad} and reference velocity U_∞. Therefore, (6.1) and (6.2) can be

https://doi.org/10.1017/jfm.2013.257 Published online by Cambridge University Press

expressed in terms of dimensionless variables, leading to

$$C_{T,rot} = 2\int_0^1 \Delta\widehat{p}_{ad}(\widehat{\sigma})\widehat{\sigma}\,\mathrm{d}\widehat{\sigma}, \tag{6.3}$$

$$C_P = 2\int_0^1 \widehat{u}(0,\sigma)\widehat{\mathscr{H}}(0,\widehat{\sigma})\widehat{\sigma}\,\mathrm{d}\widehat{\sigma}, \tag{6.4}$$

where $\Delta\widehat{p}_{ad} = 2\Delta p_{ad}/\rho U_\infty^2$ and $\widehat{\mathscr{H}} = 2\mathscr{H}/U_\infty^2$. The thrust coefficient of the duct, computed by integrating over its surface the axial force due to the pressure, reads

$$C_{T,duct} = \frac{1}{\frac{1}{2}\pi\rho U_\infty^2\sigma_{ad}^2}\oint_C p(c)\boldsymbol{n}2\pi\sigma(c)\,\mathrm{d}c\cdot\boldsymbol{i}_\zeta = -2\oint_C \widehat{\sigma}(\widehat{c})C_{p,w}(\widehat{c})\sin\beta(\widehat{c})\,\mathrm{d}\widehat{c}, \tag{6.5}$$

where $C_{p,w} = 2(p-p_\infty)/\rho U_\infty^2$ is the wall pressure coefficient and $\widehat{c} = c/\sigma_{ad}$ is the dimensionless curvilinear abscissa. Finally, the overall thrust coefficient reads

$$C_T = C_{T,rot} + C_{T,duct}. \tag{6.6}$$

In the following subsections, a few relevant applications of the present method are described. More precisely, the global and local flow characteristics are detailed both for a ducted propeller and a ducted turbine. While the results of the former configuration are presented with and without slipstream rotation, those pertaining to the turbine are only given in the general case of wake rotation, for the sake of brevity. Moreover, a validation procedure of the method is carried out with the help of asymptotic solutions. A few convergence and stability results are also provided.

6.1. *Ducted rotor without slipstream rotation*

In the special case of a contra-rotating rotor pair or of a turbomachinery stage both with $w(\zeta,\sigma) = 0$ in the wake, (5.2) returns

$$\frac{\omega_\theta(\zeta,\sigma)}{\sigma} = -\sum_{m=1}^{M}\frac{ma_m}{\Psi_{\sigma_{ad}}}\left(\frac{\Psi}{\Psi_{\sigma_{ad}}}\right)^{m-1}, \tag{6.7}$$

to be used in the iterative procedure instead of (5.2). In the downstream limit

$$\omega_\theta(\zeta\to+\infty,\sigma) = -\left.\frac{\mathrm{d}u}{\mathrm{d}\sigma}\right|_{(\zeta\to+\infty,\sigma)}. \tag{6.8}$$

Therefore, from (6.7) and from the definition of the Stokes stream function, the following second-order variable coefficients ordinary differential equation can be obtained (Conway 1998):

$$\frac{1}{\sigma}\frac{\mathrm{d}}{\mathrm{d}\sigma}\left(\frac{1}{\sigma}\frac{\mathrm{d}\Psi}{\mathrm{d}\sigma}\right) = \sum_{m=1}^{M}\frac{ma_m}{\Psi_{\sigma_{ad}}}\left(\frac{\Psi}{\Psi_{\sigma_{ad}}}\right)^{m-1}, \tag{6.9}$$

with the associated boundary conditions

$$\Psi(\zeta\to+\infty,\sigma=0) = 0, \tag{6.10a}$$

$$\Psi(\zeta\to+\infty,\sigma=\sigma_s(\zeta\to+\infty)) = \Psi_{\sigma_{ad}}. \tag{6.10b}$$

To validate the method described in § 5, equation (6.9) can be integrated, numerically or in some special cases analytically, obtaining accurate values of Ψ and u at infinity. Furthermore, a different formulation of the performance coefficients of the device can

https://doi.org/10.1017/jfm.2013.257 Published online by Cambridge University Press

Chord/rotor diameter	$chord/D$	1/2.76
Angle between the profile chord and the ζ axis	α	12.7°
Tip gap/rotor diameter	ϵ/D	1.244 %
Leading edge radial position/rotor diameter	σ_{le}/D	0.580
Leading edge axial position/rotor diameter	ζ_{le}/D	−0.111
Load magnitude parameter	$\widehat{b} = \sigma_{ad}^2 a_1 / U_\infty \Psi_{\sigma_{ad}}$	15
Advance coefficient (only with wake rotation)	J	0.5

TABLE 1. Propeller ducted with a NACA 4415 profile: geometry and operating conditions.

be obtained through the distribution of axial velocity at infinity. In fact, as a classical result of actuator disk theory, these coefficients can be related to the axial velocity at infinity. In particular, from the axial momentum and energy equations, C_T and C_P can be expressed as

$$\begin{aligned} C_T &= \frac{T}{\frac{1}{2}\pi\rho U_\infty^2 \sigma_{ad}^2} \\ &= \frac{1}{\frac{1}{2}\pi\rho U_\infty^2 \sigma_{ad}^2} \int_0^{\sigma_s(+\infty)} (u(+\infty,\sigma) - U_\infty)\rho u(+\infty,\sigma) 2\pi\sigma \, \mathrm{d}\sigma \\ &= 4 \int_0^{\widehat{\sigma}_s(+\infty)} \widehat{u}(+\infty,\widehat{\sigma})(\widehat{u}(+\infty,\widehat{\sigma}) - 1)\widehat{\sigma} \, \mathrm{d}\widehat{\sigma}, \end{aligned} \tag{6.11}$$

$$\begin{aligned} C_P &= \frac{P}{\frac{1}{2}\pi\rho U_\infty^3 \sigma_{ad}^2} \\ &= \frac{1}{\frac{1}{2}\pi\rho U_\infty^3 \sigma_{ad}^2} \int_0^{\sigma_s(+\infty)} (H(+\infty,\sigma) - H_\infty)\rho u(+\infty,\sigma) 2\pi\sigma \, \mathrm{d}\sigma \\ &= 2 \int_0^{\widehat{\sigma}_s(+\infty)} \widehat{u}(+\infty,\widehat{\sigma})(\widehat{H}(+\infty,\widehat{\sigma}) - \widehat{H}_\infty)\widehat{\sigma} \, \mathrm{d}\widehat{\sigma}. \end{aligned} \tag{6.12}$$

With the help of (5.1), equation (6.12) can be integrated analytically to give

$$C_P = \frac{4\Psi_{\sigma_{ad}}}{U_\infty^3 \sigma_{ad}^2} \sum_{m=0}^{M} \frac{a_m}{m+1}. \tag{6.13}$$

In the special case of a wake without swirl, the pressure jump across the disk is directly related to the load through

$$\mathscr{H} = \frac{\Delta p_{ad}(\sigma)}{\rho}, \tag{6.14}$$

thus obtaining

$$\Delta\widehat{p}_{ad}(\sigma) = \widehat{\mathscr{H}}(\Psi) = \frac{2}{U_\infty^2} \sum_{m=0}^{M} a_m \left(\frac{\Psi}{\Psi_{\sigma_{ad}}} \right)^m, \tag{6.15}$$

to be used in (6.3) in order to calculate the rotor thrust coefficient $C_{T,rot}$.

https://doi.org/10.1017/jfm.2013.257 Published online by Cambridge University Press

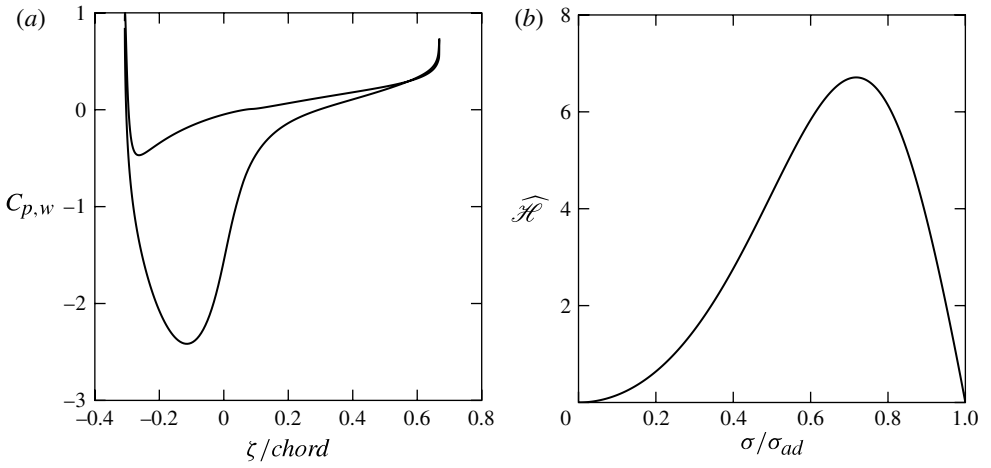


FIGURE 1. Propeller ducted with a NACA 4415 profile with $\widehat{b} = 15$: (*a*) duct wall pressure coefficient; (*b*) radial distribution of load.

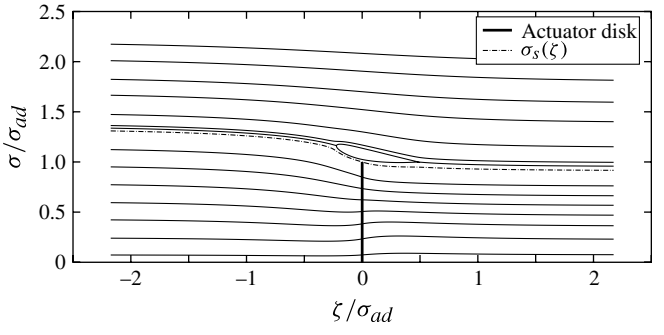


FIGURE 2. Propeller ducted with a NACA 4415 profile with $\widehat{b} = 15$: streamlines.

For the simple case of a load distribution of the type

$$\mathscr{H}(\Psi) = a_1 \left[\frac{\Psi}{\Psi_{\sigma_{ad}}} - \left(\frac{\Psi}{\Psi_{\sigma_{ad}}} \right)^2 \right], \tag{6.16}$$

the solution procedure applied to a rotor ducted with a NACA 4415 (see table 1 for details) returns the wall pressure coefficient and the dimensionless load radial distribution reported in figure 1. While the shape of the computed dimensionless load radial distribution obtained with the simple equation (6.16) bears a good physical resemblance to that for a typical propeller, its magnitude (i.e. the particular value of $\widehat{b}$) has been selected in order to enhance the performance of the duct. In more detail, the value of $\widehat{b} = 15$ leads to a position of the front stagnation point in the leading edge area, so that undesired suction or pressure side velocity peaks are avoided. This is clearly visible from the duct wall pressure coefficient of figure 1(*a*).

Figure 2 shows the streamlines over the ducted actuator disk, denoted by the thick solid line. The dot-dashed line defines the slipstream edge $\sigma_s(\zeta)$. The no-penetration condition over the duct, enforced in the iterative process through (5.17), is clearly

https://doi.org/10.1017/jfm.2013.257 Published online by Cambridge University Press

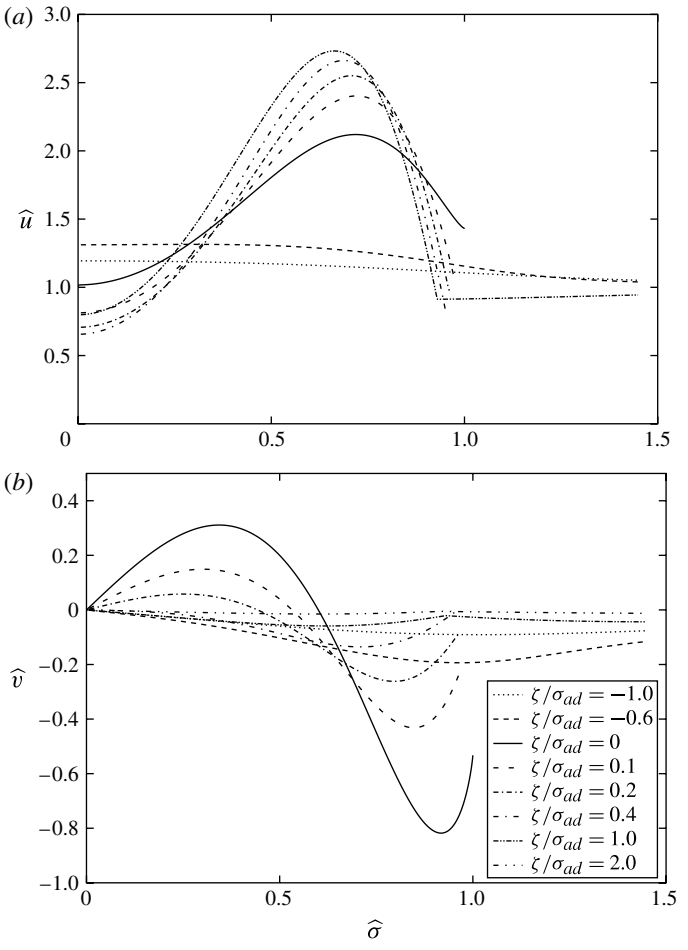


FIGURE 3. Propeller ducted with a NACA 4415 profile with $\widehat{b} = 15$: (*a*) $\widehat{u}$ and (*b*) $\widehat{v}$ radial distributions at different axial stations.

satisfied by the solution, as evident by the two streamlines flowing just above and below the profile. Moreover, the position of the front stagnation point is readily localized by the dividing streamline. Finally, the flow leaves the profile smoothly at the trailing edge according to the Kutta condition requirement.

Figure 3 shows the radial distributions of axial and radial dimensionless velocity at different axial stations (see also figure 2 as a graphical aid to locate them). As a first remark, both distributions highlight the typical propeller slipstream contraction whose magnitude is largely dictated by the disk load. In fact the radial velocity is essentially negative in the outer part of the slipstream. Moreover, the axial velocity excess increases in the streamwise direction, while the radial velocity simultaneously approaches zero. The above features further prove the contraction of the slipstream and the establishment of the wake contraction in the downstream limit, respectively. Finally, the total, axial and radial velocity contours are shown in figure 4(*a–c*).

The slipstream $\sigma_s(\zeta)$ at different iterations and the convergence history are given in figure 5(*a*,*b*), respectively. In the latter, the residue is defined as the absolute value of the difference between two successive slipstream radii evaluated at $\zeta = 5\sigma_{ad}$,

https://doi.org/10.1017/jfm.2013.257 Published online by Cambridge University Press

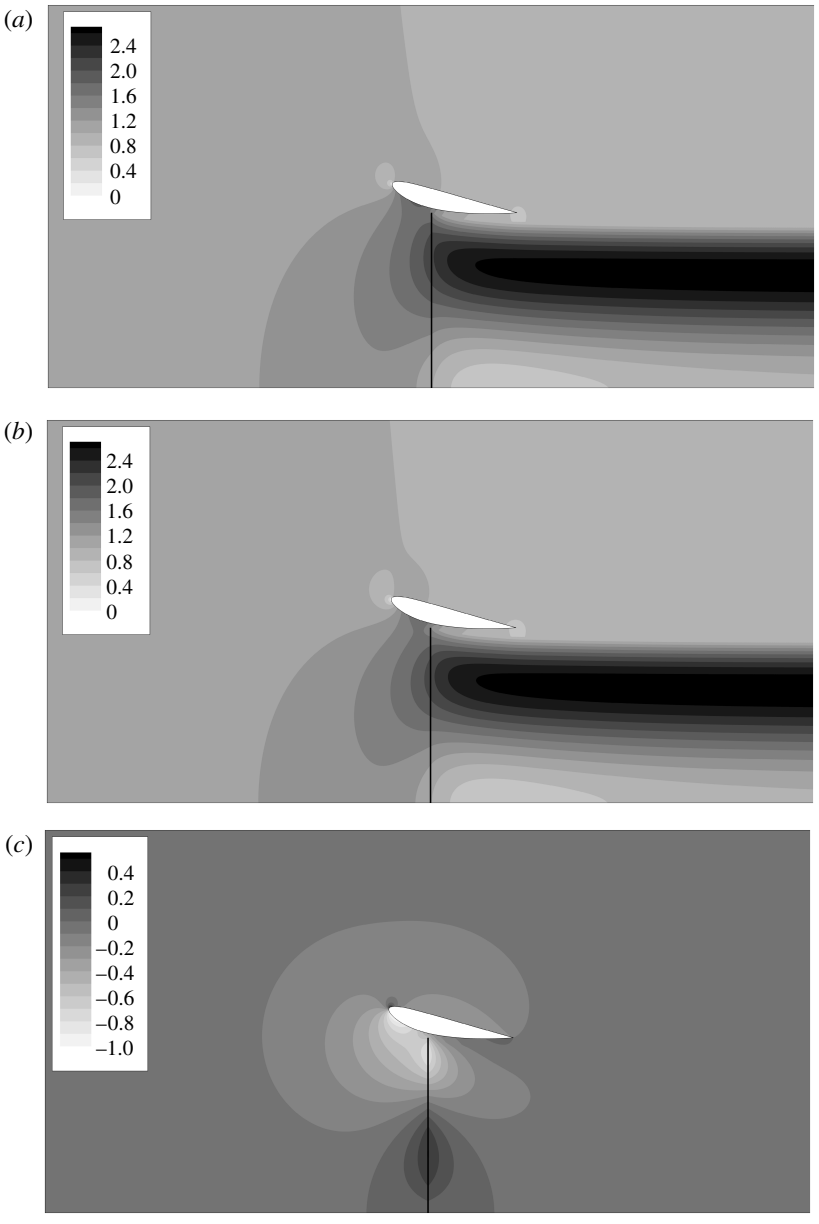


FIGURE 4. Propeller ducted with a NACA 4415 profile with $\widehat{b} = 15$: (*a*) total, (*b*) axial and (*c*) radial velocity contours.

normalized with σ_{ad}. The number of iterations needed to reach convergence with different values of $\widehat{b}$ is detailed in table 2. The convergence of the iterative process is very rapid for moderate loads and worsens for higher loads, so that under-relaxation is typically needed in order to preserve stability. In particular, the value of the slipstream radius at each iteration is updated through the relation

$$\sigma_s(\zeta) = \sigma_s(\zeta)|_{old} + [\sigma_s(\zeta)|_{new} - \sigma_s(\zeta)|_{old}]\,\omega_{rf}, \tag{6.17}$$

https://doi.org/10.1017/jfm.2013.257 Published online by Cambridge University Press

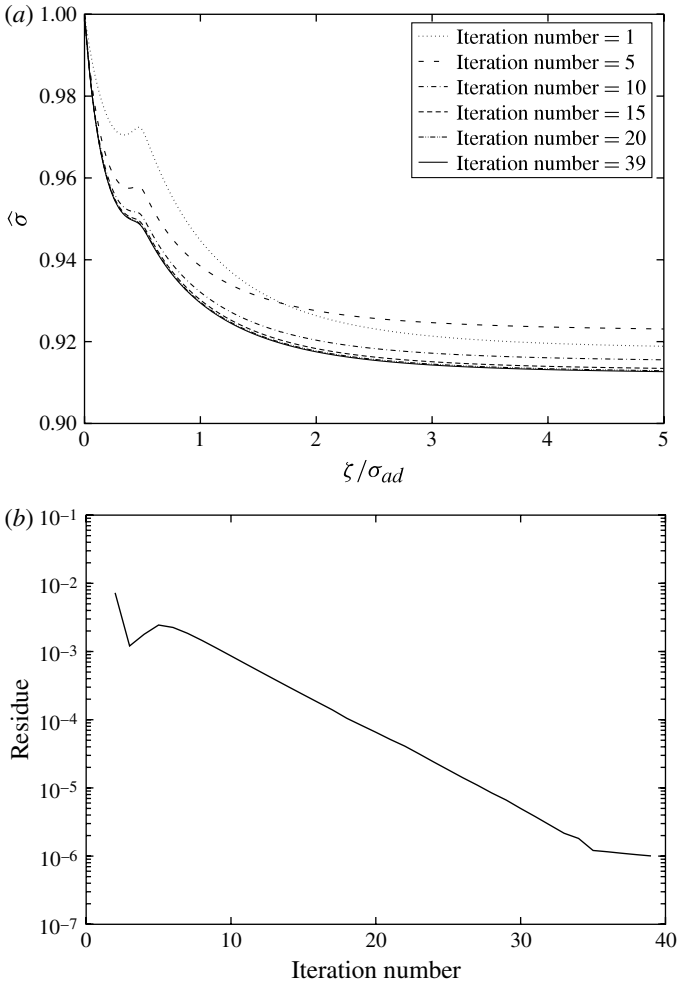


FIGURE 5. Propeller ducted with a NACA 4415 profile with $\widehat{b} = 15$: convergence analysis showing (*a*) slipstream at different iterations and (*b*) residue.

$\widehat{b}$	$\omega_{rf} = 1$	$\omega_{rf} = 1/3$	$\omega_{rf} = 1/6$
5	12	27	47
10	32	32	64
15	178	39	73
20	Not converged	39	78

TABLE 2. Propeller ducted with a NACA 4415 profile with $\widehat{b} = 15$: number of iterations needed to reach convergence with different loads and relaxation factors ω_{rf}.

where ω_{rf} is the relaxation factor. The latter should be fixed minimizing the number of iterations needed to reach convergence; table 2 shows typical values.

https://doi.org/10.1017/jfm.2013.257 Published online by Cambridge University Press

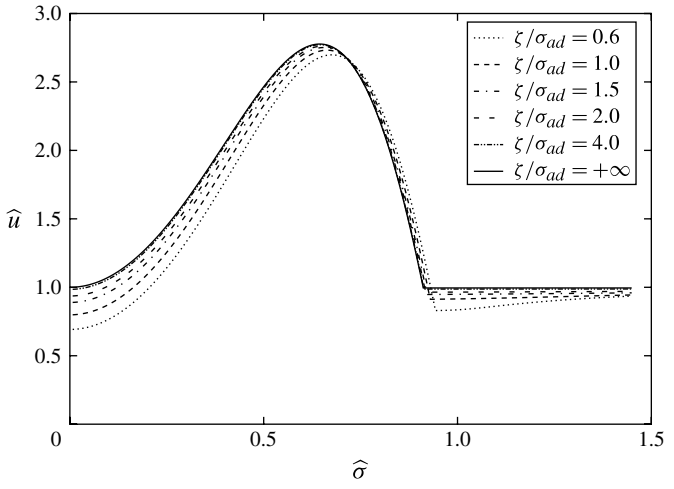


FIGURE 6. Propeller ducted with a NACA 4415 profile with $\widehat{b} = 15$: approach of the $\widehat{u}$ radial distribution to the asymptotic one.

C_T	$C_{T,rot}$	$C_{T,duct}$	C_P	η
4.62	4.14	0.48	8.01	0.58

TABLE 3. Propeller ducted with a NACA 4415 profile with $\widehat{b} = 15$: performance coefficients.

In the special case of a parabolic load distribution, like the one in (6.16), equation (6.9) reduces to

$$\frac{1}{\sigma}\frac{\mathrm{d}}{\mathrm{d}\sigma}\left(\frac{1}{\sigma}\frac{\mathrm{d}\Psi}{\mathrm{d}\sigma}\right) = \frac{U_\infty \widehat{b}}{\sigma_{ad}^2}\left[1 - 2\left(\frac{\Psi}{\Psi_{\sigma_{ad}}}\right)\right]. \tag{6.18}$$

The analytical solution of the above equation, with the associated boundary conditions (6.10), is detailed in Conway (1998). Figure 6 compares the dimensionless axial velocity distribution computed by the iterative scheme described in § 5 with the analytical one obtained by solving (6.18). It is worth noting that at four propeller radii downstream of the disk the axial velocity field has almost reached the theoretical profile at infinity. The above result provides a validation of the method and gives evidence of an appropriate control of the related numerical issues. Finally, the global performance coefficients for the NACA 4415 case are listed in table 3.

6.2. *Ducted rotor with slipstream rotation*

In the case with swirl, the tangential velocity $w(\zeta, \sigma)$ is computed through the angular momentum equation (2.8), which, using (5.1), yields

$$\widehat{w}(\zeta, \sigma) = \frac{w(\zeta, \sigma)}{U_\infty} = \frac{J}{\pi}\frac{\sigma_{ad}}{\sigma}\frac{1}{U_\infty^2}\sum_{m=0}^{M} a_m \left(\frac{\Psi}{\Psi_{ad}}\right)^m. \tag{6.19}$$

https://doi.org/10.1017/jfm.2013.257 Published online by Cambridge University Press

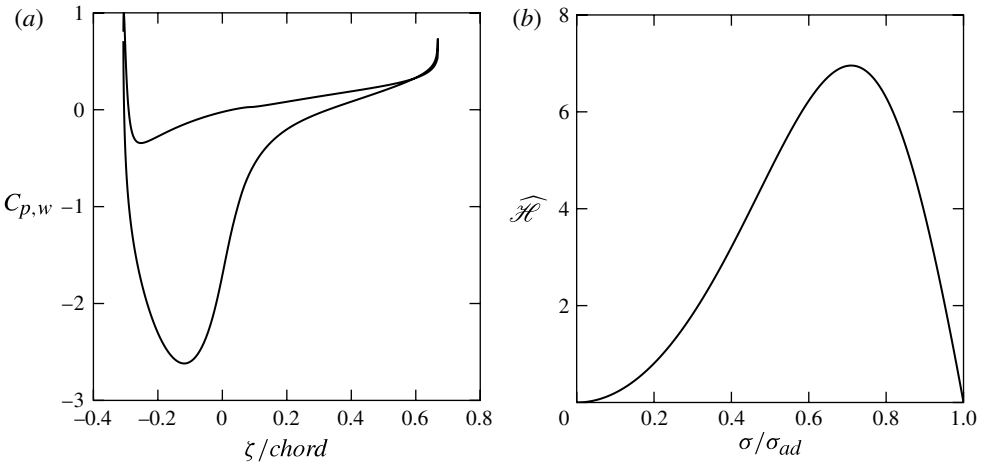


FIGURE 7. Propeller ducted with a NACA 4415 profile with $\widehat{b} = 15$ and $J = 0.5$: (*a*) duct wall pressure coefficient; (*b*) radial distribution of load.

Chord/rotor diameter	$chord/D$	0.513
Angle between the profile chord and the ζ axis	α	−5.0°
Tip gap/rotor diameter	ϵ/D	1.039 %
Leading edge radial position/rotor diameter	σ_{le}/D	0.559
Leading edge axial position/diameter	ζ_{le}/D	−0.15
Load magnitude parameter	$\widehat{b} = \sigma_{ad}^2 a_1/U_\infty \Psi_{\sigma_{ad}}$	−2
Tip speed ratio	λ	2π

TABLE 4. Turbine ducted with a NACA 5415 profile: geometry and operating conditions.

Recalling the expression for the θ component of vorticity (5.2) and replacing in (5.2) its asymptotic value $\omega_\theta(\zeta \to +\infty, \sigma)$ given by (6.8), the following second-order variable coefficients ordinary differential equation is obtained:

$$\frac{1}{\sigma}\frac{\mathrm{d}}{\mathrm{d}\sigma}\left(\frac{1}{\sigma}\frac{\mathrm{d}\Psi}{\mathrm{d}\sigma}\right) = \left[\frac{J^2}{\pi^2}\left(\frac{\sigma_{ad}}{\sigma}\right)^2 \frac{1}{U_\infty^2}\sum_{m=0}^{M} a_m \left(\frac{\Psi}{\Psi_{\sigma_{ad}}}\right)^m - 1\right] \sum_{m=1}^{M} \frac{m a_m}{\Psi_{\sigma_{ad}}}\left(\frac{\Psi}{\Psi_{\sigma_{ad}}}\right)^{m-1}, \quad (6.20)$$

with the associated boundary conditions (6.10). Like in the case without slipstream rotation, the above equation can be integrated to give an accurate solution for Ψ at downstream infinity, and furthermore this result can be used to compute the performance coefficients of the device. In particular, the equivalent formula to (6.11) is

$$C_T = 2\int_0^{\widehat{\sigma}_s(+\infty)} \left[\frac{2\pi}{J}\widehat{\sigma}\widehat{w}(+\infty, \widehat{\sigma}) + (\widehat{u}(+\infty, \widehat{\sigma}) - 1)^2 - \widehat{w}^2(+\infty, \widehat{\sigma})\right] \widehat{\sigma}\, \mathrm{d}\widehat{\sigma}, \quad (6.21)$$

while (6.12)–(6.13) are still valid.

The pressure jump across the disk is related to the load radial distribution through $\mathscr{H} = \Delta p_{ad}(\sigma)/\rho + w^2(0^+, \sigma)/2$. The latter equation, elaborated with the help of (5.1)

https://doi.org/10.1017/jfm.2013.257 Published online by Cambridge University Press

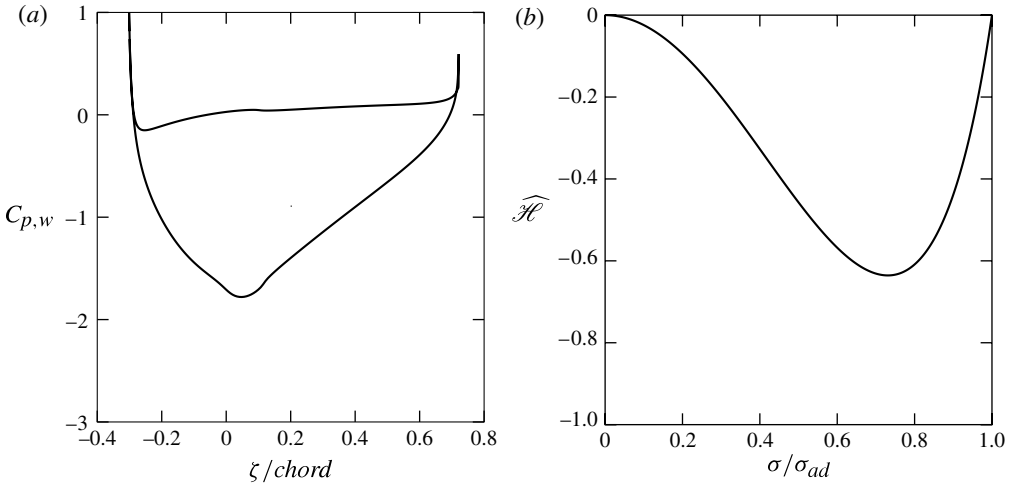


FIGURE 8. Turbine ducted with a NACA 5415 profile with $\widehat{b} = -2$ and $\lambda = 2\pi$: (*a*) duct wall pressure coefficient; (*b*) radial distribution of load.

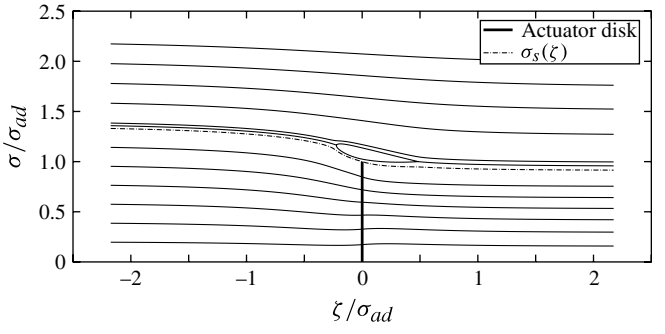


FIGURE 9. Propeller ducted with a NACA 4415 profile with $\widehat{b} = 15$ and $J = 0.5$: streamlines.

and (2.8), yields

$$\Delta\widehat{p}_{ad}(\sigma) = \frac{1}{U_\infty^2}\sum_{m=0}^{M} a_m \left(\frac{\Psi}{\Psi_{\sigma_{ad}}}\right)^m \left[2 - \frac{J^2}{\pi^2}\frac{\sigma_{ad}^2}{\sigma^2}\frac{1}{U_\infty^2}\sum_{m=0}^{M} a_m \left(\frac{\Psi}{\Psi_{\sigma_{ad}}}\right)^m\right], \qquad (6.22)$$

to be used in (6.3) in order to calculate the rotor thrust coefficient $C_{T,rot}$.

With reference to the geometry and operating conditions detailed in tables 1 and 4, figures 7 and 8 show the wall pressure coefficient and the dimensionless load radial distribution for a propeller ducted with a NACA 4415 and a turbine ducted with a NACA 5415, respectively. The particular value of $\widehat{b} = 15$ ($\widehat{b} = -2$ in the turbine case) leads again to a position of the front stagnation point lying in the leading edge area (see figures 7*a* and 8*a*). This latter feature of the flow, the streamline pattern and the converging–diverging shape of the wake are shown in figures 9 and 10. As for the case without swirl, the no-penetration and Kutta condition compliance can also be appreciated. Figures 11–14 present the radial distributions of dimensionless axial, radial and tangential velocities at different axial stations. Concerning the through-flow

https://doi.org/10.1017/jfm.2013.257 Published online by Cambridge University Press

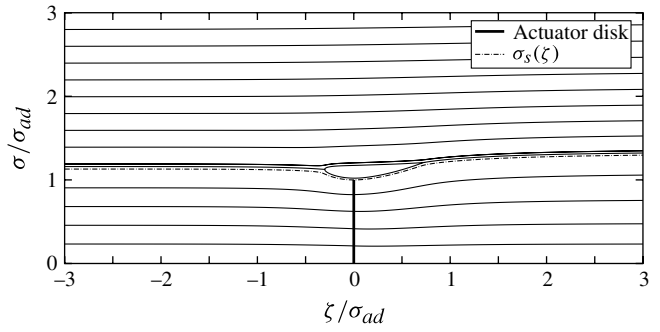


FIGURE 10. Turbine ducted with a NACA 5415 profile with $\widehat{b} = 2$ and $\lambda = 2\pi$: streamlines.

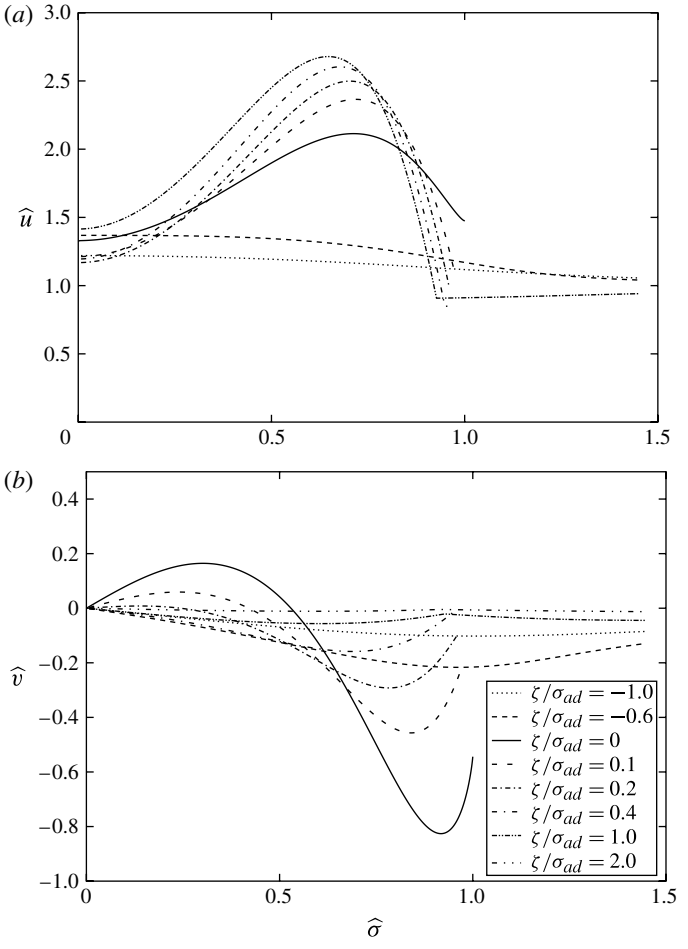


FIGURE 11. Propeller ducted with a NACA 4415 profile with $\widehat{b} = 15$ and $J = 0.5$: (*a*) $\widehat{u}$ and (*b*) $\widehat{v}$ radial distributions at different axial stations.

velocity distributions, the same features as pointed out when discussing figure 3 are also detectable in figures 11 and 13. The tangential velocity falls to zero at the ζ axis and at the slipstream edge, since the load is prescribed to vanish there.

https://doi.org/10.1017/jfm.2013.257 Published online by Cambridge University Press

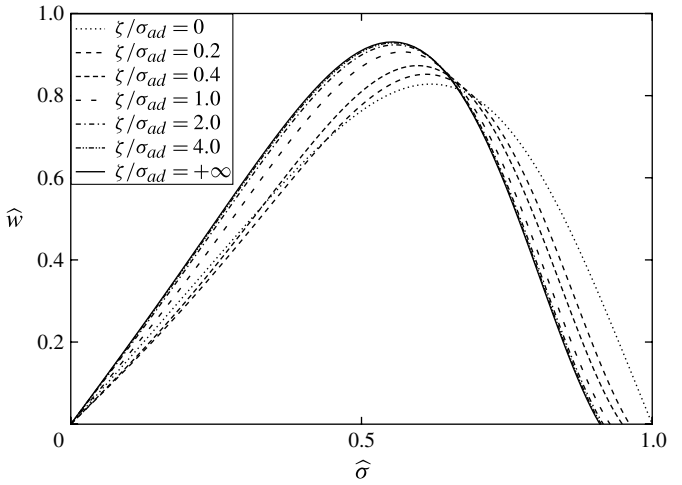


FIGURE 12. Propeller ducted with a NACA 4415 profile with $\widehat{b} = 15$ and $J = 0.5$: $\widehat{w}$ radial distribution at different axial stations.

C_T	$C_{T,rot}$	$C_{T,duct}$	C_P	η
4.57	4.02	0.55	8.60	0.53

TABLE 5. Propeller ducted with a NACA 4415 profile with $\widehat{b} = 15$ and $J = 0.5$: performance coefficients.

The dimensionless radii where $w = 0$ in figures 12 and 14 locate the slipstream edge contraction (divergence) moving downstream. Using the angular momentum conservation law (2.8), the variation of the $\widehat{w}$ profile as ζ increases can be easily explained. In fact, with reference to the propeller case, the tangential velocity along a streamline increases as ζ increases, a consequence of the load $\mathscr{H}$ invariance along the streamline while the latter is converging. Finally, the contours of total, axial and radial velocity are shown in figures 15 and 16.

The slipstream $\sigma_s(\zeta)$ at different iterations and the convergence history are given in figure 17(*a*,*b*). There are no considerable effects of the slipstream rotation on the convergence and stability of the iterative process.

Equation (6.20) can be numerically integrated to obtain an accurate solution for Ψ at infinity; then $\widehat{u}(+\infty, \sigma)$ and $\widehat{w}(+\infty, \sigma)$ can be computed through the definition of the Stokes stream function and (6.19), respectively. To validate the slipstream rotation implementation, a sequence of $\widehat{u}$ and $\widehat{w}$ profiles, as ζ increases, are shown together with the theoretical distribution at infinity in figures 12, 14 and 18. At four–six disk diameters downstream, the velocity distributions have nearly attained their corresponding asymptotic values. Finally, the global performance coefficients are listed in tables 5 and 6.

https://doi.org/10.1017/jfm.2013.257 Published online by Cambridge University Press

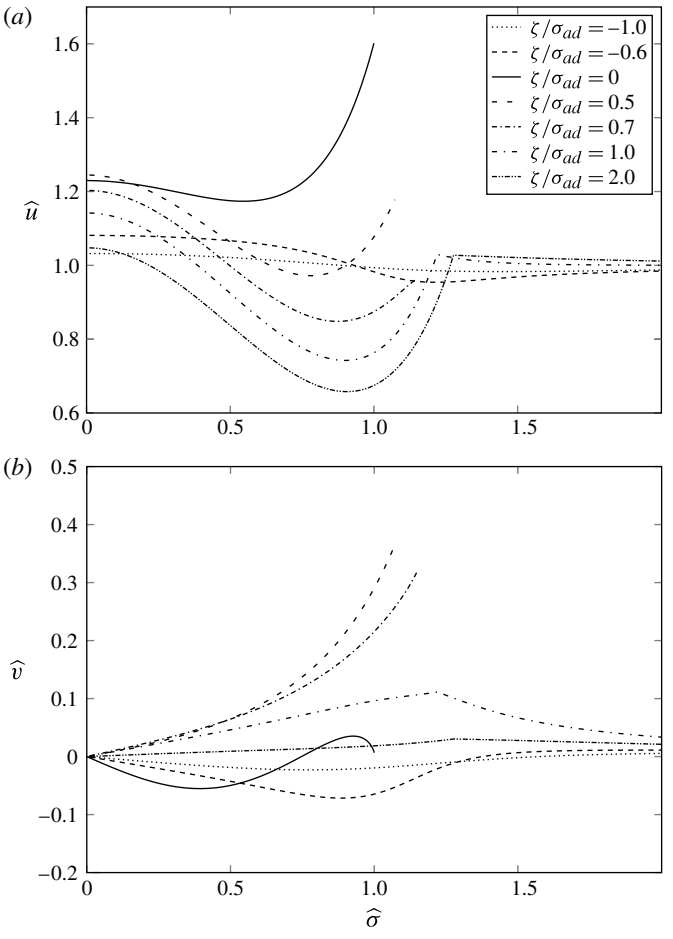


FIGURE 13. Turbine ducted with a NACA 5415 profile with $\widehat{b} = -2$ and $\lambda = 2\pi$: (*a*) $\widehat{u}$ and (*b*) $\widehat{v}$ radial distributions at different axial stations.

C_T	$C_{T,rot}$	$C_{T,duct}$	C_P
−0.64	−0.43	−0.21	−0.54

TABLE 6. Turbine ducted with a NACA 5415 profile with $\widehat{b} = -2$ and $\lambda = 2\pi$: performance coefficients.

6.3. *Comparison between open and ducted rotor*

As mentioned in the introduction, the task of the duct is to improve the performance of the device. In particular, for a turbine with radius σ_{ad} and immersed in a uniform flow with free stream velocity U_∞, the effect of the duct is to increase the power output or in dimensionless form the power coefficient C_P, that is, the ratio between the extracted and the available power. In more detail, for a turbine without slipstream rotation, the load at the disk can be expressed through (6.14). Consequently, the thrust and the

https://doi.org/10.1017/jfm.2013.257 Published online by Cambridge University Press

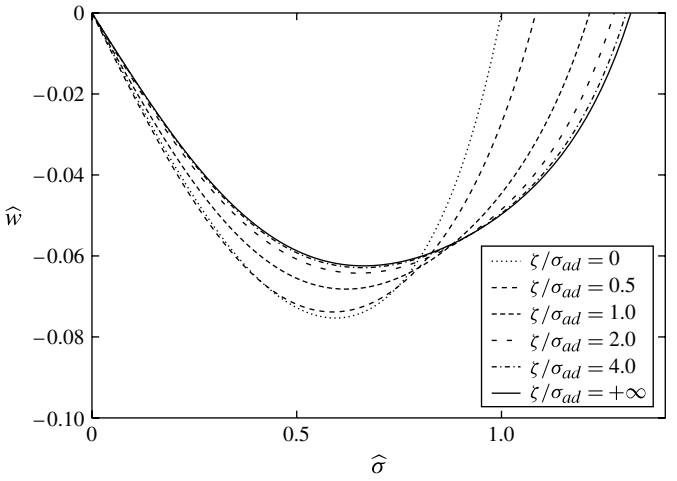


FIGURE 14. Turbine ducted with a NACA 5415 profile with $\widehat{b} = -2$ and $\lambda = 2\pi$: $\widehat{w}$ radial distributions at different axial stations.

power associated with the rotor infinitesimal surface element of area $\mathrm{d}A_{rot} = 2\pi\sigma\,\mathrm{d}\sigma$ are $\mathrm{d}T_{rot} = \Delta p_{ad}(\sigma)\,\mathrm{d}A_{rot} = \rho\mathscr{H}(\sigma)\,\mathrm{d}A_{rot}$ and $\mathrm{d}P = \mathscr{H}(\sigma)\,\mathrm{d}\dot{m} = (u(0,\sigma) + U_\infty)\,\mathrm{d}T_{rot}$, respectively. Finally, the local power coefficient is

$$\mathrm{d}C_P = (\widehat{u}(0,\widehat{\sigma}) + 1)\mathrm{d}C_{T,rot}. \tag{6.23}$$

The last equation shows that the power coefficient is the product of two terms related to the mass flow and the load, respectively. Hansen, Sorensen & Flay (2000) and de Vries (1979) analysed the effects of placing a duct around a turbine without slipstream rotation through a one-dimensional theoretical analysis and CFD results. In these works it is found that, for a ducted and open turbine with the same load, the presence of the duct can increase the mass flow passing through the disk, thus increasing the power coefficient (see equation (6.23)).

In the following, the previous issue is analysed through the method described in this paper. Consider a turbine ducted with a NACA 5415 (see table 4 for geometrical details) without swirl and an open turbine with the same load radial distribution (see figure 19(*a*)). The results for this last configuration are obtained through the standard actuator disk method of Conway (1998). Because the radial loads $\mathscr{H}(\sigma)$ of the two turbines are the same, they also have the same $\mathrm{d}C_{T,rot}$ and $C_{T,rot}$. However, since the presence of the duct increases the mass flow through the ducted rotor (see figure 20), the power coefficient value of the ducted turbine is greater than that of the open turbine (see table 7). Moreover, the C_P value of the ducted turbine is also greater than $16/27 \simeq 0.593$, which is the well-known maximum theoretical C_P value achievable by an open turbine (Betz limit).

Figure 20 also shows that, in order to obtain an increase of the mass flow, the duct slipstream $\sigma_s(\zeta)$ has to be more divergent for $\zeta > 0$ and more convergent for $\zeta < 0$ in comparison with the open rotor configuration. So in the special case of a ducted turbine, the latter result points out the features of the method (which naturally takes into account the shape of the slipstream) in comparison with the one-dimensional theory where the effects of the slipstream divergence is neglected.

https://doi.org/10.1017/jfm.2013.257 Published online by Cambridge University Press

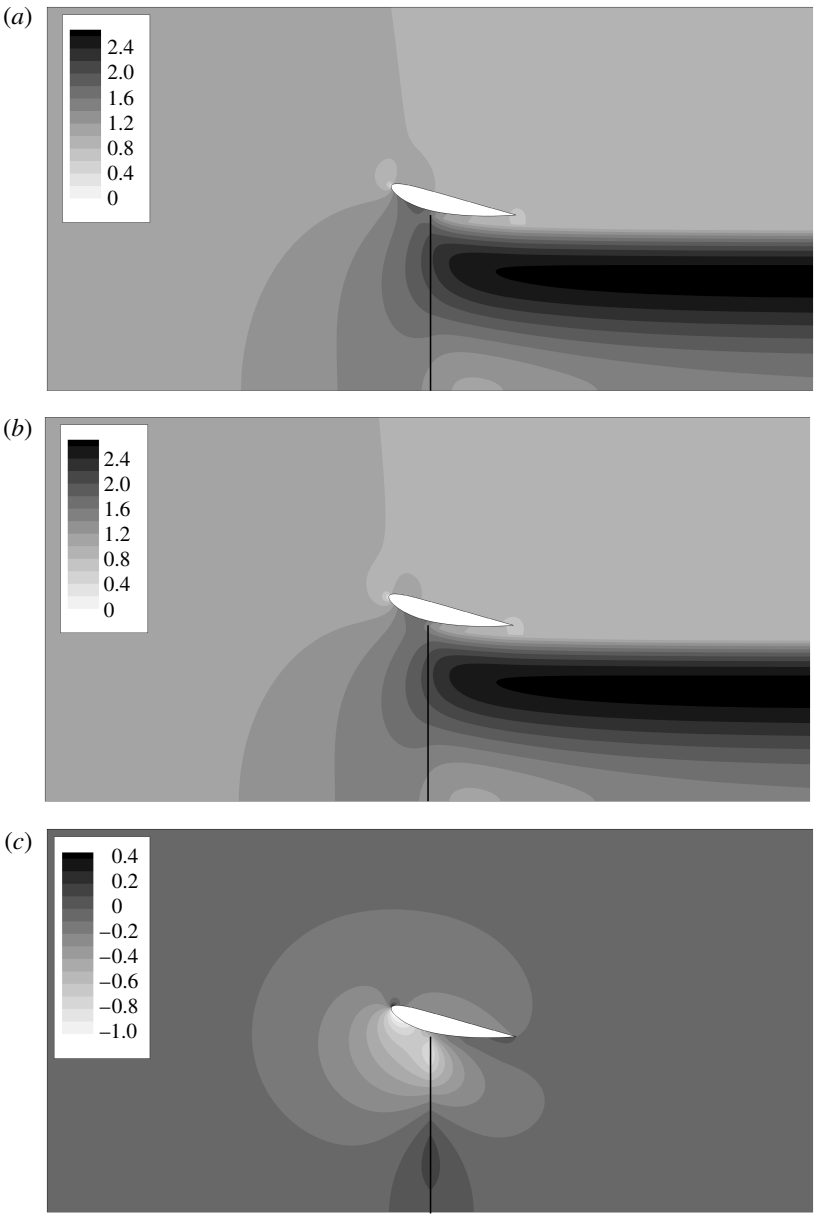


FIGURE 15. Propeller ducted with a NACA 4415 profile with $\widehat{b} = 15$ and $J = 0.5$: (*a*) total, (*b*) axial and (*c*) radial velocity contours.

For a propeller the main task of the duct is to increase the efficiency, notwithstanding the propulsive thrust required by the carrier. Hence, the efficiency being $\eta = C_T/C_P$, a well-designed duct enables the propeller to achieve a lower value of C_P without altering the total thrust coefficient C_T. Consider, then, an open propeller without slipstream rotation and with a parabolic load radial distribution. The performance coefficients obtained when setting $\widehat{b} = 22.025$ are detailed in table 8. These results are obtained using the standard actuator disk method of Conway (1998).

https://doi.org/10.1017/jfm.2013.257 Published online by Cambridge University Press

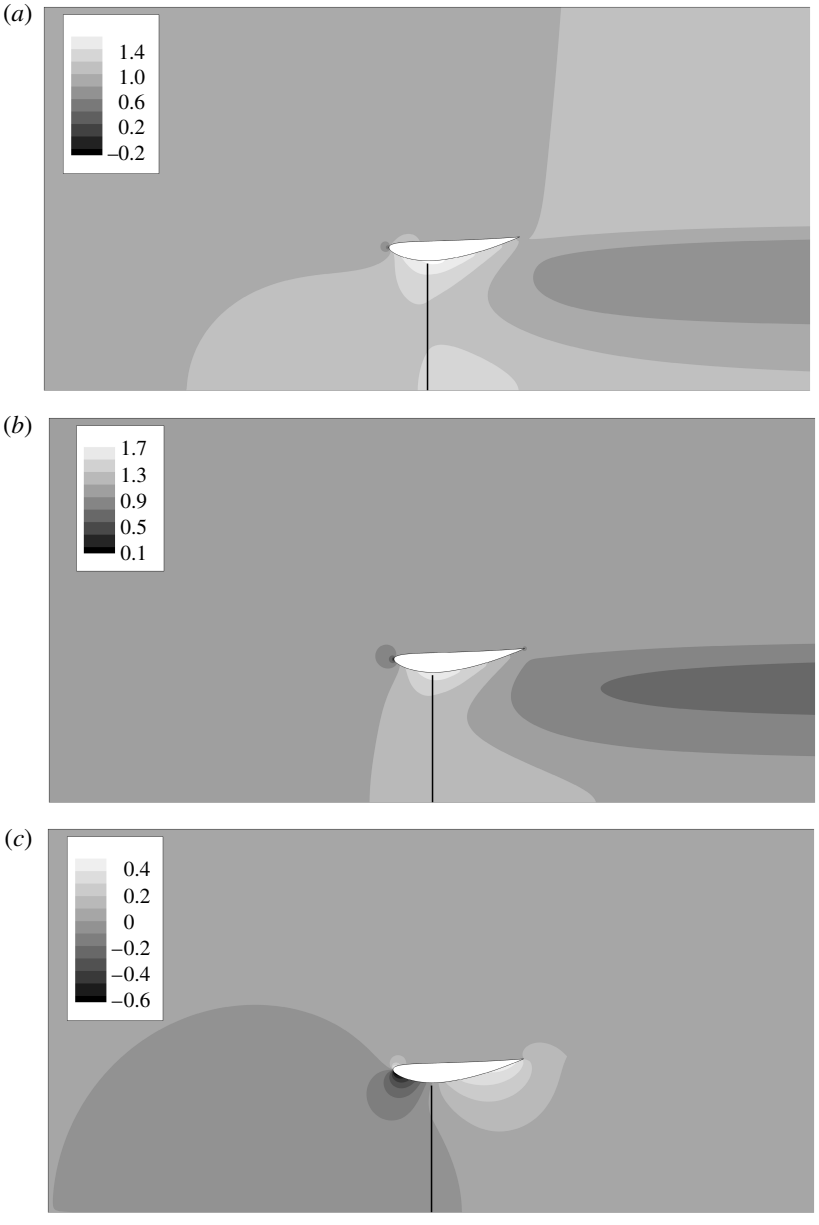


FIGURE 16. Turbine ducted with a NACA 5415 profile with $\widehat{b} = -2$ and $\lambda = 2\pi$: (*a*) total, (*b*) axial and (*c*) radial velocity contours.

Consider now a propeller ducted with a NACA 5415 (see table 9 for geometrical details) with the same radius σ_{ad} and radial load distribution ($\widehat{b} = 14.0$) as the open propeller. Such a propeller achieves the same C_T value as the open one (see table 8), but now the thrust is split up between the duct and the rotor. In turn, the power coefficient C_P is lower than that of the open propeller alone and this results in a higher efficiency. Figures 21 and 19(*b*) show the slipstream edge and the load radial distribution for the open and the ducted propeller. From figure 21, it is easily inferred

https://doi.org/10.1017/jfm.2013.257 Published online by Cambridge University Press

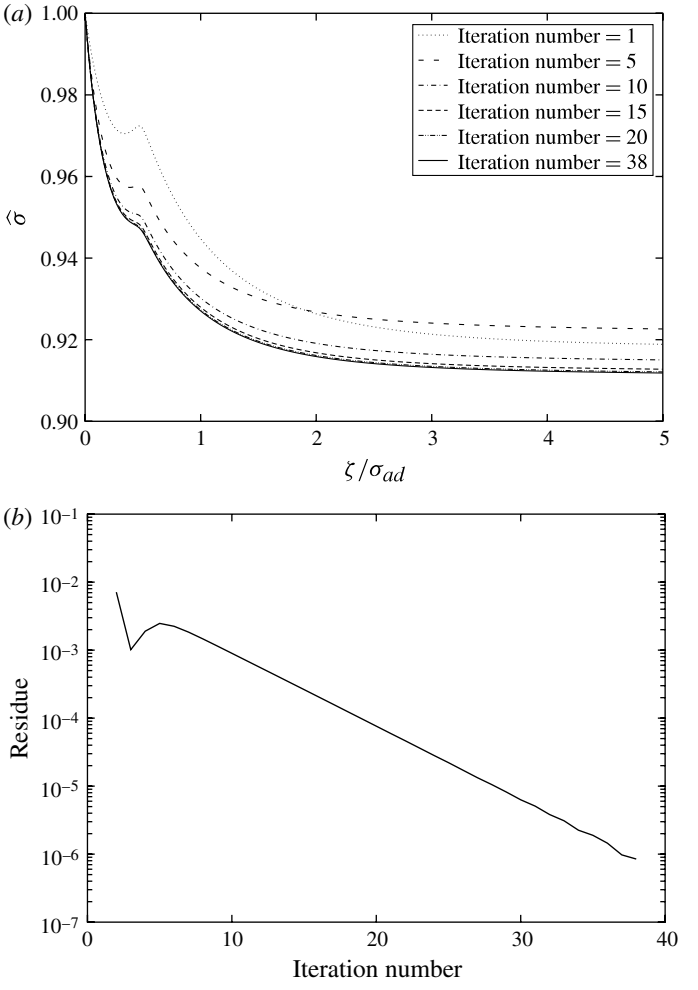


FIGURE 17. Propeller ducted with a NACA 4415 profile with $\widehat{b} = 15$ and $J = 0.5$: convergence analysis showing (*a*) slipstream at different iterations and (*b*) residue.

	Open turbine	Ducted turbine	$\Delta C_P/C_{P,open}$
$C_{T,rot}$	−0.62	−0.62	
C_T	−0.62	−0.82	
$C_{T,duct}$	—	−0.20	
C_P	−0.46	−0.61	32.61 %

TABLE 7. Comparison of the open and ducted turbine performance coefficients.

that the ducted propeller swallows a greater mass flow. Despite this latter feature, its overall power, or rather its power coefficient C_P, is lower than the open propeller one, because of the rotor load reduction (see figure 19*b*).

https://doi.org/10.1017/jfm.2013.257 Published online by Cambridge University Press

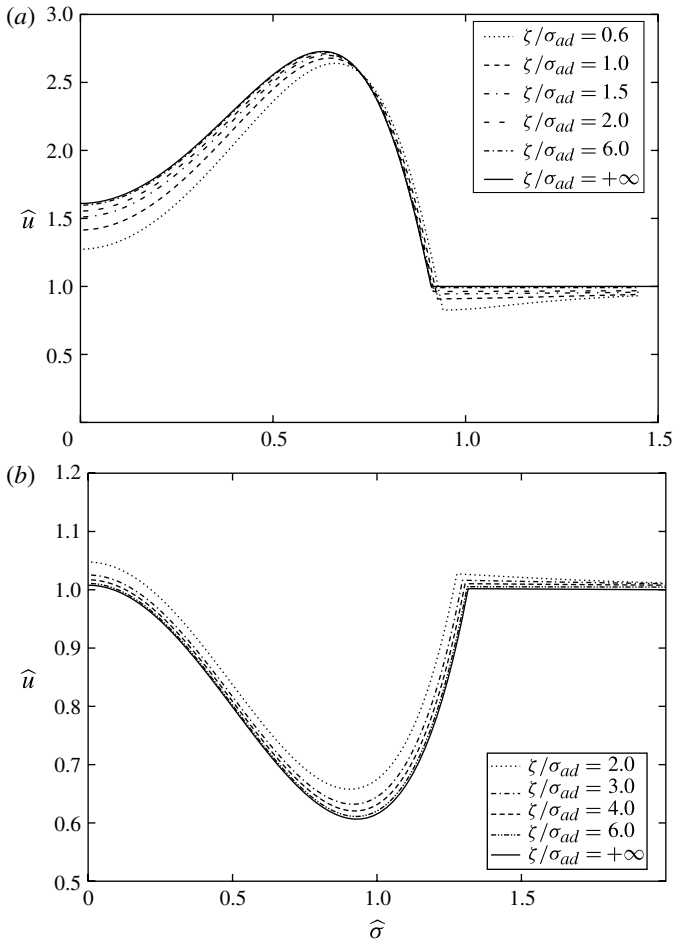


FIGURE 18. Rotors with slipstream rotation: $\widehat{u}$ distributions at different axial stations. (*a*) Propeller ducted with a NACA 4415 profile with $\widehat{b} = 15$ and $J = 0.5$. (*b*) Turbine ducted with a NACA 5415 profile with $\widehat{b} = -2$ and $\lambda = 2\pi$.

	Open propeller	Ducted propeller	$\Delta\eta/\eta_{open}$
C_T	5.22	5.22	
$C_{T,rot}$	5.22	4.31	
$C_{T,duct}$	—	0.91	
C_P	9.90	9.14	
η	0.53	0.57	7.55 %

TABLE 8. Comparison of the open and ducted propeller performance coefficients.

7. Conclusions

An extension to ducted rotors of the nonlinear actuator disk theory of Conway (1998) has been presented. In particular, an exact solution of the inviscid axisymmetric flow generated by a heavily loaded ducted rotor and a cost-effective semi-analytical

https://doi.org/10.1017/jfm.2013.257 Published online by Cambridge University Press

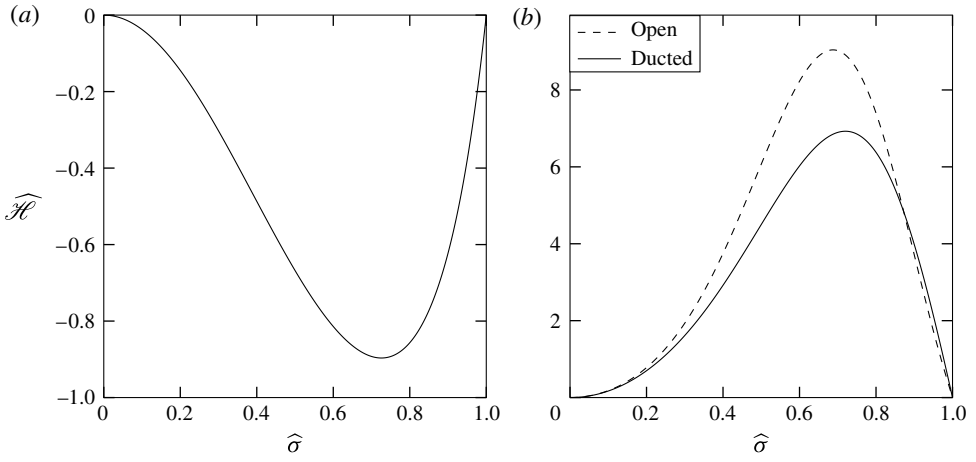


FIGURE 19. Load radial distribution for open and ducted rotors: (*a*) turbines; (*b*) propellers.

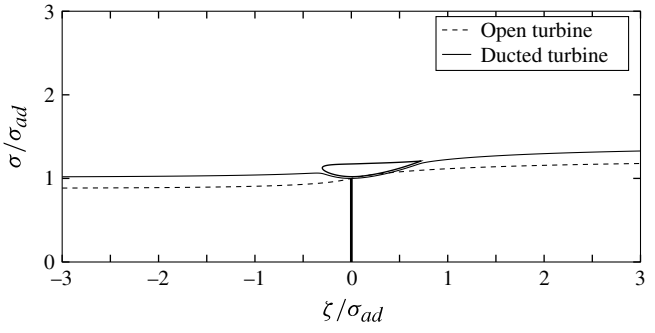


FIGURE 20. Comparison of the open and the ducted turbine slipstream edge.

Axial chord/rotor diameter	$chord_\zeta/D$	0.5
Angle between the profile chord and the ζ axis	α	12.7°
Tip gap/rotor diameter	ϵ/D	1.019 %
Leading edge radius/rotor diameter	σ_{le}/D	0.625
Load magnitude parameter	$\widehat{b} = \sigma_{ad}^2 a_1/U_\infty \Psi_{\sigma_{ad}}$	14

TABLE 9. Propeller ducted with a NACA 5415 profile: geometry and operating condition.

solution procedure of the resulting equation are detailed. The solution being exact, the proper shape of the slipstream, whether converging or diverging, is naturally accounted for, even for heavy loads. The solution procedure can handle rotor wake rotation, radial load distributions and ducts of general shape. Furthermore, the method preserves the fully coupled nature of the solution, duly taking into account the nonlinear mutual interaction between the duct and the rotor. The solution is expressed as a triple integral over the radial and axial coordinates and over the allowed values of the separation constant of the eigensolutions of the Laplace equation in cylindrical coordinates. Two of these integrals are exactly evaluated, while the integration in the axial direction

https://doi.org/10.1017/jfm.2013.257 Published online by Cambridge University Press

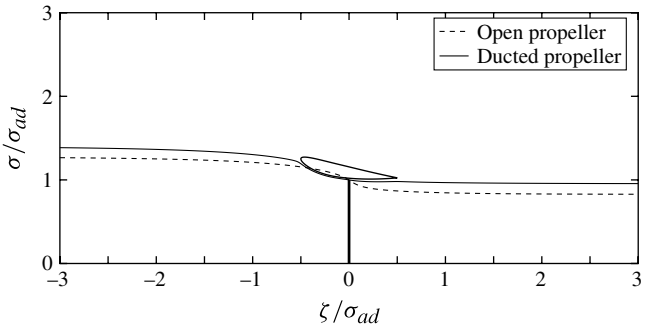


FIGURE 21. Comparison of the open and the ducted propeller slipstream edge.

is performed through numerical quadrature, with an extremely reduced computational cost. Therefore, the method is well suited for the design and/or analysis of ducted rotors for marine, wind and aeronautical applications.

The computer code is freely available on contacting the authors.

Acknowledgements

The authors would like to thank Professor A. Vacca, Professor R. Tognaccini, Professor J. T. Conway and Professor S. Miranda for their helpful suggestions.

REFERENCES

ANDERSON, J. D. 2001 *Fundamentals of Aerodynamics*, 3rd edn. McGraw-Hill.

BALTAZAR, J. & FALCÃO DE CAMPOS, J. A. C. 2009 On the modelling of the flow in ducted propellers with a panel method. In *Proceedings of the 1st International Symposium on Marine Propulsors*.

BASSET, A. B. 1888 *A Treatise on Hydrodynamics*, Vol. II. Deighton Bell.

BATCHELOR, G. K. 1967 *An Introduction to Fluid Dynamics*. Cambridge University Press.

BRESLIN, J. P. & ANDERSEN, P. 1994 *Hydrodynamics of Ship Propellers*. Cambridge University Press.

FALCÃO DE CAMPOS, J. A. C. 1983 On the calculation of ducted propeller performance in axisymmetric flows. PhD thesis, Delft University of Technology.

CARLTON, J. 2007 *Marine Propellers and Propulsion*. Butterworth-Heinemann.

ÇELIK, F., GÜNER, M. & EKINCI, S. 2010 An approach to the design of ducted propeller. *Scientia Iranica, Trans. B: Mech. Engng* **17** (5), 406–417.

CHAPLIN, H. R. 1964 A method for numerical calculation of slipstream contraction of a shrouded impulse disk in the static case with application to other axisymmetric potential flow problems. *Tech. Rep.* 1857. David Taylor Model Basin.

CONWAY, J. T. 1995 Analytical solutions for the actuator disk with variable radial distribution of load. *J. Fluid Mech.* **297**, 327–355.

CONWAY, J. T. 1998 Exact actuator disk solutions for non-uniform heavy loading and slipstream contraction. *J. Fluid Mech.* **365**, 235–267.

CONWAY, J. T. 2000 Analytical solutions for the Newtonian gravitational field induced by matter within axisymmetric boundaries. *Mon. Not. R. Astron. Soc.* **316** (3), 540–554.

DICKMANN, H. E. & WEISSINGER, J. 1955 Beitrag zur Theorie optimaler Düsenschrauben (Kortdüsen). *Jahrb. Schiffbautechn.* **49**, 452–486.

GIBSON, I. S. 1972 Application of vortex singularities to ducted propellers. PhD thesis, University of Newcastle upon Tyne.

https://doi.org/10.1017/jfm.2013.257 Published online by Cambridge University Press

GIBSON, I. S. & LEWIS, R. I. 1973 Ducted propeller analysis by surface vorticity and actuator disk theory. In *Proceedings of the Symposium on Ducted Propeller*. Royal Institute of Naval Architects.

GRADSHTEYN, I. S. & RYZHIK, I. M. 1980 *Tables of Integrals, Series and Products*. Academic Press.

GREENBERG, M. D. & POWERS, S. R. 1970 Nonlinear actuator disk theory and flow field calculations, including nonuniform loading. NASA *Tech. Rep.* CR-1672.

VAN GUNSTEREN, L. A. 1973 A contribution to the solution of some specific ship propulsion problems. PhD thesis, Delft University of Technology.

HANSEN, M. O. L., SORENSEN, N. N. & FLAY, R. G. 2000 Effect of placing a diffuser around a wind turbine. *Wind Energy* **3**, 207–213.

HORLOCK, J. H. 1978 *Actuator Disc Theory*. McGraw-Hill.

JACOB, K. & RIEGELS, F. W. 1963 The calculation of the pressure distributions over aerofoil sections of finite thickness with and without flaps and slats. *Z. Flugwiss.* **11** (9), 357–367.

KERWIN, J. E., KINNAS, S. A., LEE, J. T. & SHIH, W. 1987 A surface panel method for the hydrodynamic analysis of ducted propellers. *Trans. Soc. Nav. Archit. Mar. Engrs* **95**.

LAMB, H. 1932 *Hydrodynamics*. Cambridge University Press.

LEWIS, R. I. 1991 *Vortex Element Methods for Fluid Dynamic Analysis of Engineering Systems*. Cambridge University Press.

MARTENSEN, E. 1959 Berechnung der Druckverteilung an Gitterprofilen in ebener Potentialströmung mit einer Fredholmschen Integralgleichung. *Arch. Rat. Mech. Anal.* **3**, 235–270.

NYIRI, A. & BARANYI, L. 1983 Numerical method for calculating the flow around a cascade of aerofoils. In *Proceedings of VII International JSME Symposium on Fluid Machinery and Fluidics*, vol. 2.

RYAN, P. G. & GLOVER, E. J. 1972 A ducted propeller design method: a new approach using surface vorticity distribution techniques and lifting line theory. *Trans. R. Inst. Nav. Archit.* **114**, 545–563.

SONINE, N. J. 1880 Recherches sur les fonction cylindriques et le développement des fonctions continues en séries. *Math. Ann.* **16** (1), 1–80.

DE VRIES, O. 1979 *Fluid Dynamic Aspects of Wind Energy Conversion*. AGARDograph No. 243.

WILKINSON, D. H. 1967*a* A numerical solution of the analysis and design problems for the flow past one or more aerofoils or cascades. *Tech. Rep.* 3545. A.R.C.

WILKINSON, D. H. 1967*b* The calculation of rotational, non-solenoidal flows past two-dimensional aerofoils and cascades. *Tech. Rep.* W/M(6C). English Electric, M.E.L.

WU, T. Y. 1962 Flow through a heavily loaded actuator disc. *Schiffstechnik* **9**, 134–138.

https://doi.org/10.1017/jfm.2013.257 Published online by Cambridge University Press